Research Square

Preprints are preliminary reports that have not undergone peer review.
They should not be considered conclusive, used to inform clinical practice,
or referenced by the media as validated information.

Integrated SMR-Adsorption System for Blue Hydrogen Production: CFD Analysis of CO_2 Capture and Hydrogen Purification

Abdelwahab N. Allam
King Fahd University of Petroleum and Minerals
Naef A.A. Qasem
naefqasem@kfupm.edu.sa
King Fahd University of Petroleum and Minerals
Medhat A. Nemitallah
King Fahd University of Petroleum and Minerals
Rached Ben-mansour
King Fahd University of Petroleum and Minerals
Mohamed A. Habib
King Fahd University of Petroleum and Minerals

Research Article

Keywords: Blue Hydrogen Production, Steam Methane reforming, Adsorption, Carbon capture, CFD

Posted Date: August 25th, 2026

DOI: https://doi.org/10.21203/rs.3.rs-10279933/v1

License: This work is licensed under a Creative Commons Attribution 4.0 International License.
Read Full License

Additional Declarations: No competing interests reported.

Integrated SMR-Adsorption System for Blue Hydrogen Production: CFD Analysis of CO_2 Capture and Hydrogen Purification

Abdelwahab N. Allam[a], Naef A.A. Qasem[b,c*], Medhat A. Nemitallah[b,d], Rached Ben-Mansour[a,e], Mohamed A. Habib[a,d]

[a] Department of Mechanical Engineering, King Fahd University of Petroleum & Minerals (KFUPM), Dhahran 31261, Saudi Arabia

[b] Department of Aerospace Engineering, King Fahd University of Petroleum & Minerals (KFUPM), Dhahran 31261, Saudi Arabia

[c] Interdisciplinary Research Center for Aviation and Space Exploration, King Fahd University of Petroleum and Minerals (KFUPM), Dhahran 31261, Saudi Arabia

[d] Interdisciplinary Research Center for Hydrogen Technologies and Carbon Management, King Fahd University of Petroleum & Minerals (KFUPM), Dhahran 31261, Saudi Arabia

[e] Interdisciplinary Research Center for Sustainable Energy Systems, King Fahd University of Petroleum and Minerals (KFUPM), Dhahran 31261, Saudi Arabia

[*]Corresponding author: naefqasem@kfupm.edu.sa (Naef A.A. Qasem)

Abstract

Blue hydrogen is a low-carbon energy carrier produced from natural gas when carbon emissions are captured. The primary method of producing it is steam methane reforming (SMR), a process that separates hydrogen from natural gas but generates large quantities of carbon dioxide. This study proposes an integration process combining SMR, a heat exchanger, and a fixed-bed adsorption unit to enhance hydrogen production *via* carbon capture after reforming. A computational fluid dynamics (CFD) analysis was developed using the transient, axisymmetric, two-dimensional ANSYS Fluent model, validated against experimental data from the literature. A previously validated SMR model was used by sequentially coupling the reformer outlet to a downstream cooler/condensate knock-out unit, followed by a fixed-bed adsorption column. The adsorption system performance is evaluated under various operating conditions, including heat exchanger outlet temperature (298 - 448 K), adsorption pressure (0 - 20 bar), CO_2/H_2O ratio (25/75 to 75/25%), and gas hourly space velocity (GHSV: 100-500 h^{-1}). The adsorption unit is analyzed using a breakthrough curve approach. The results showed that lower temperature delayed CO_2 breakthrough markedly (680 s at 298 K vs. 70 s at 448 K); higher pressure increased capacity (q_{CO_2} rose from 0.75 to 2.4 mol/kg when pressure increased from 0 to 20 bar); higher CO_2 in the feed accelerated saturation (breakthrough advanced from 850 s at 25 % CO_2 to 520 s at 75 % CO_2); and increasing GHSV shortened bed life (680 s at 100 h^{-1} vs. 100 s at 500 h^{-1}). The results showed that the best overall operating conditions for long bed life and high capture were low temperature, high

pressure, moderate CO_2 content, and low GHSV, which improve CO_2 capture and H_2 purity, offering design guidance for efficient blue hydrogen production systems.

Keywords:

Blue Hydrogen Production; Steam Methane reforming; Adsorption; Carbon capture; CFD

Nomenclature

Symbol	***Description***	***Abbreviation***	***Meaning***
C	Concentration (mol/m³)	CH_4	Methane
D	Mass diffusivity (m²/s)	H_2O	Water (steam)
d	Diameter	CO_2	Carbon dioxide
q	Adsorbed amount (mol/kg)	H_2	Hydrogen
q*	Equilibrium adsorbed amount (mol/kg)	CO	Carbon monoxide
GHSV	Gas Hourly Space Velocity (h^{-1})	UDF	User-Defined Function
P	Pressure (bar)	UDS	User-Defined Scalar
T	Temperature (K)	MOF	Metallic Organic Framework
ΔH	Heat of adsorption (J/mol)	CCS	Carbon Capture and Storage
k	Mass transfer coefficient (s^{-1}) (LDF)	SER	Sorption-Enhanced Reforming
h	Convective heat-transfer coefficient (W/(m²·K))	LDF	Linear Driving Force
Nu	Nusselt number (-)	S/C	Steam-to-Carbon
Pr	Prandtl number (-)	SMR	Steam Methane Reforming
Ra	Rayleigh number (-)	CFD	Computational Fluid Dynamics
n	Toth exponent (-)	PSA	Pressure Swing Adsorption
$\vec{g}$	Gravity vector (m/s²)	GHSV	Gas Hourly Space Velocity
C_2	Inertial resistance coefficient (m^{-1})	WGS	Water Gas Shift
K	Permeability (m^2)	BPNN	backpropagation neural network
M	Molecular weight (kg/mol)	***Greek symbol***	***Description***
S	Momentum source term (N/m³)	ε	Porosity (-)
E	Total energy (J/m^3)	ρ	Density (kg/m^3)
v	Velocity (m/s)	μ	Dynamic viscosity (pa.s)
x	Axial position (m)	ε_w	Wall emissivity (wall) (-)
Y	Mass fraction (-)	σ	Stefan -Boltzmann constant (W/m^2K^4)
y	Mole fraction (-)	$\bar{\bar{\tau}}$	Stress tensor (N/m²)

Subscripts

Subscript	***Description***	***Subscript***	***Description***
ads	Adsorbed phase	inlet	Inlet
amb	Ambient	Outlet / o	Outlet
eff	Effective	g	Gas
eq	At equilibrium	max	Maximum
ext	External	p	Particle
f	Film (average)	s	Solid
i	Species	w	Wall

1. Introduction

The global energy landscape is undergoing a significant transformation, with hydrogen emerging as a pivotal clean energy carrier due to its versatility and zero-carbon combustion profile. Its applications span industrial processes, transportation, and power generation, making it a cornerstone of future sustainable energy systems [1], [2], To meet the escalating demand, hydrogen must be produced through diverse pathways, including steam methane reforming (SMR), renewable-powered electrolysis (green hydrogen), biomass gasification, partial oxidation, and thermochemical cycles [3], [4], [5]. Among these, SMR remains the most commercially mature and cost-effective method for large-scale production, owing to its established infrastructure and scalability [6]. Meanwhile, green hydrogen offers a near-zero-emission route when derived from solar, wind, or hydroelectric sources, and blue hydrogen, integrating carbon capture with conventional routes, bridges the gap toward a low-carbon transition.

Despite its economic and operational advantages, SMR is subject to thermodynamic irreversibilities that limit its overall efficiency. Rosen [7] conducted a comprehensive energy and exergy analysis of SMR-based hydrogen production, revealing that while energy losses appeared substantial, exergy destruction was relatively modest, with an overall exergetic efficiency of 78.5%. The primary losses were attributed to the combustion stage and the CO_2 removal step, highlighting the critical role of exergy assessment in pinpointing process bottlenecks and guiding optimization strategies. In a typical SMR process, methane reacts with steam over a nickel-based catalyst at elevated temperatures (700-1000 °C) and pressures (5-20 bar), yielding a synthesis gas composed of H_2, CO, and CO_2 [8], [9]. To maximize hydrogen yield, the effluent is subsequently directed to a water-gas shift (WGS) reactor, where CO reacts with steam-often over a high-temperature catalyst such as chromium-promoted iron oxide—to produce additional H_2 and CO_2. The final purification stage, commonly employing pressure swing adsorption (PSA), is responsible for a significant hydrogen loss, typically around 20%, due to adsorption inefficiencies. The underlying reactions (Eqs. 1–3) are equilibrium-limited and predominantly endothermic, necessitating careful thermal management to drive conversion [10], [11]:

$$CH_4 + H_2O \leftrightarrow CO + 3H_2 \qquad \Delta H_{rx} = 206\ kJ/mol \qquad \text{Endothermic} \qquad (1)$$

$$CO + H_2O \leftrightarrow CO_2 + H_2 \qquad \Delta H_{rx} = -41.15\ kJ/mol \qquad \text{Exothermic} \qquad (2)$$

$$CH_4 + 2H_2O \leftrightarrow CO_2 + 4H_2 \qquad \Delta H_{rx} = 165\ kJ/mol \qquad \text{Endothermic} \qquad (3)$$

The supremacy of SMR in large-scale hydrogen production remains due to its low costs and high hydrogen purity. But they generate a gas stream containing CO_2 and residual CO, so purification is required to make this gas usable in various applications, including fuel cells and ammonia synthesis [12]. Separation of CO_2 from H_2-rich streams is also critical to hydrogen production systems intended to reduce carbon emissions and allow carbon capture and storage (CCS). Depending upon the location of the operation, several CO_2 capture techniques are used. In pre-combustion capture operations, which most occur in autothermal reforming or gasification, CO_2 is

physically removed from shifted syngas using chemical solvents [13] or PSA [14]. In post-combustion capture operations, which can be applied to SMR furnace flue gas, solid adsorbents or chemical solvents [15], [16] are used. Sorption Enhanced Reforming (SER) combines CO_2 removal with the reforming process using solid sorbents such as CaO. This will shift the equilibrium towards favoring hydrogen production [17]. Emerging membrane-based separation technology has the possibility of providing compact, selective gas separation using polymeric or palladium membranes [18]. Hybrid systems combining PSA, membrane, or solvent-based methods further increase CO_2 capture efficiencies in clean hydrogen production [19], [20].

In terms of CO_2 removal through adsorption-based technologies, there were many research investigations focused on materials like zeolite, activated carbon, and metal organic framework (MOF) [21], [22]. At specific pressures and temperatures, each material exhibits significant selectivity for CO_2. Cavaliere [23] presented an overview of hydrogen purification technologies for water electrolysis. It described a three-step process: pretreatment, first stage separation, and second stage purification. The chapter stated that although the majority of the industry uses PSA for first-stage separation due to its efficiency and industrial maturity, alternative separation processes exist. For ultra-high purity hydrogen (below 1 ppm impurities), advanced techniques such as cryogenic adsorption and palladium membrane separation are explored. The work underscores the importance of matching purification strategies to application-specific purity and operational requirements, with ongoing advancements aimed at improving recovery and energy efficiency.

Previous research has demonstrated the effectiveness of PSA in the hydrogen purification [24], [25]. However, the integration of PSA with the SMR and heat exchangers remains underexplored. Study by Krótki et al. [26] conducted a comprehensive review of PSA technology for hydrogen purification from syngas and WGS syngas mixtures. The study emphasizes PSA's dominance in industrial applications due to its efficiency, maturity, and scalability. Important operational factors affecting PSA performance were identified, including flow designs, cycle sequences, pressure settings, and adsorbent selection. Furthermore, the authors propose an experimental framework that integrates breakthrough adsorption studies and dynamic PSA process evaluations to enhance hydrogen recovery and purity. Different published papers discuss models used in adsorption. One such study is presented by Chilev et al. [27], who compared eight adsorption isotherm models, including Langmuir, Toth, Sips, Freundlich, Jovanovic, OBMR, UNILAN, and Potential Theory to evaluate their accuracy in describing the adsorption equilibria of pure hydrogen, nitrogen, and methane gases on activated carbon JX101. Experimental data at three temperatures (283 K, 298 K, and 313 K) were used, and the models were assessed via nonlinear regression in MATLAB. Thermodynamic parameters like pseudo-saturation vapor pressure and molar volume were estimated using the Dubinin and Do models, respectively. The study concludes that most models, except the Freundlich model for nitrogen and methane, provide high correlations ($R^2 > 0.99$) with experimental data. The results highlight the strong adsorbate-adsorbent interactions, especially for methane, and affirm the suitability of temperature-dependent models for accurate adsorption

characterization. Ben-Mansour et al. [28] used CFD modeling and experimental methods to study the effect of humidity on the separation of CO_2 from CO_2/N_2 gas mixtures using Mg-MOF-74. A two and three-dimensional model developed in ANSYS Fluent was validated against experimental breakthrough data. Results showed that Mg-MOF-74 exhibits high CO_2 adsorption capacity under dry conditions, but the presence of water vapor significantly reduces CO_2 uptake by up to 47% at 9.1% RH and 373 K due to competitive adsorption on active sites. The study concluded that drying flue gas before CO_2 capture is crucial to maintaining high adsorption efficiency.

Kim et al. [29] conducted a comprehensive experimental and theoretical investigation of the separation of hydrogen from a mixture of carbon dioxide and hydrogen using a five-step, single-column PSA process with zeolite 5A. The PSA cycle, optimized for H_2 purification following steam reforming, demonstrated that H_2 could be concentrated from 70% in the feed to 99.99% purity with a recovery of 67.5%. The study examined the effects of adsorption time and purge-to-feed ratio, showing that higher purge ratios improve H_2 purity but reduce recovery. The process dynamics were accurately predicted using a linear driving force (LDF) model incorporating nonlinear Langmuir-Freundlich isotherms and energy balances, validating the PSA's effectiveness for bulk H_2/CO_2 separation. Lopes et al. [30] investigated the use of modified activated carbon for hydrogen purification from SMR off-gases using PSA and vacuum PSA processes. Through a series of multicomponent breakthrough experiments (including binary H_2-CO_2, ternary H_2-CO_2-CO, and quinary H_2-CO_2-CO-CH_4-N_2), the study validated the extended Virial isotherm and a detailed fixed-bed mathematical model. A 10-step one-column VPSA experiment achieved 99.981% hydrogen purity with 81.6% recovery and an adsorbent productivity of 101 mol. $H_2 \cdot kg^{-1} \cdot day^{-1}$. Further simulations demonstrated that optimized step times and multiple pressure equalizations can enhance hydrogen recovery (>75%) while maintaining CO levels below 10 ppm and hydrogen purity above 99.99%. Ahn et al. [31] explored layered two- and four-bed pressure swing adsorption (PSA) systems for hydrogen recovery from coal gas mixtures containing low H_2 concentrations and high levels of CO_2 and N_2. Using beds packed with activated carbon and zeolite 5A, the study examined the dynamic performance of PSA cycles under varying pressures, purge-to-feed (P/F) ratios, and adsorbent configurations. The two-bed PSA system showed trade-offs between purity and recovery, with zeolite-rich beds enhancing H_2 purity but reducing recovery. In contrast, the four-bed PSA system achieved better overall performance, producing hydrogen with 96-99.5% purity and 71-85% recovery. The results highlighted that the zeolite layer acts as a nitrogen separator in two-bed systems and as a purifier in four-bed systems.

Schell et al. [32] studied the adsorption behavior for pure and binary mixtures of CO_2, H_2, and N_2 on commercial activated carbon (AP3-60) under conditions relevant to pre-combustion capture of CO_2 in hydrogen production systems. Using a magnetic suspension balance, the study measured adsorption equilibria over a wide range of temperatures (25-140 °C) and pressures (up to 21 MPa), and fit the data to Langmuir and Sips isotherms. Henry's constants and isosteric heats were derived to evaluate the adsorption strength and thermal effects. Binary adsorption predictions using extended Sips models and Ideal Adsorbed Solution Theory (IAST) were compared with

experimental data, with IAST providing better agreement. The study demonstrated that CO_2 is strongly adsorbed over H_2 and N_2, confirming the activated carbon's suitability for CO_2/ H_2 separation in PSA processes. For pre-combustion CO_2 capture in PSA systems, Casas et al. [33] assessed two novel MOF-based adsorbents: USO-2-Ni MOF and UiO-67/MCM-41 hybrid. Breakthrough experiments and detailed process simulations were used to characterize and compare these materials against activated carbon. The USO-2-Ni MOF demonstrated the best overall separation performance and productivity, while the UiO-67/MCM-41 hybrid showed higher productivity than activated carbon, albeit with slightly lower separation efficiency. Multi-objective optimization revealed that material properties, such as adsorption capacity and packing density, significantly affect process outcomes and highlighted the importance of particle formulation in scaling MOFs for industrial PSA applications. Using a patented activated carbon adsorbent (TDA AMS-19), Subraveti et al. [34] recently created and improved several innovative pressure swing adsorption (PSA) cycles for pre-combustion CO_2 capture. The study focused on achieving U.S. Department of Energy targets of >95% CO_2 purity and >90% recovery while minimizing energy consumption and maximizing productivity. Among six PSA configurations evaluated, three met the DOE criteria, with the best-performing 10-step cycle achieving a low energy consumption of 95.7 kWh/ton of CO_2 captured at 3.3 mol $CO_2/m^3_{\text{adsorbent}}$/s. The authors highlighted the benefits of using steam purge and multi-objective genetic algorithm optimization to tailor PSA cycles for enhanced CO_2 capture performance.

Recently, Streb and Mazzotti [35] investigated the potential of using zeolite 13X for simultaneous carbon dioxide capture and hydrogen purification during low-carbon hydrogen production. They conducted pioneering experiments and evaluated H_2 and CH_4 adsorption curves to study how these two gases react under different conditions. Their validated 1D column model effectively predicted both mass and heat transfer dynamics, showing robustness across different operational parameters. CO_2 showed the strongest adsorption, CH_4 moderate, and H_2 the weakest. Among the modeling approaches, RAST and IAST provided the most accurate descriptions of competitive adsorption, supporting their use in designing efficient adsorption-based separation systems. Zhang et al. [36] explored the optimization of a layered-bed PSA process for hydrogen purification by modeling it with Aspen Adsorption™ and applying the Box-Behnken Design method. Using a mixture containing H_2, CH_4, CO, N_2, and CO_2, they investigated how changes in the time of the adsorption, time of pressure equalization, and the purge-to-feed ratio influenced system performance. The findings revealed trade-offs: longer adsorption enhanced recovery but reduced purity, while longer equalization improved purity at the productivity cost. BBD-based optimization identified the ideal operating conditions for achieving high purity of hydrogen and efficient performance, confirming the approach's reliability for PSA process tuning. Recently, Zhang et al. [37] investigated the use of a triple layer made of UTSA-16, activated carbon, and zeolite 5A to improve hydrogen purification by PSA. Simulations of adsorption isotherms and breakthrough curves validated the superior performance of placing UTSA-16 furthest from the inlet, achieving 99.99% hydrogen purity, 62.08% recovery, and 7.22 mol/(kg·h) productivity. To further optimize the PSA cycle, the study developed and compared two machine learning models: a backpropagation neural network

(BPNN) and BPNN optimized by a genetic algorithm (BPNN-GA). Results showed that the BPNN-GA model significantly outperformed conventional BPNN, with lower prediction errors and higher correlation with experimental data, confirming its robustness for predicting and optimizing PSA process parameters.

Previous work presented a detailed numerical investigation of hydrogen production via SMR in a porous nickel catalytic reactor, focusing on the optimization of key operating parameters and radiation heat-transfer models[38]. To simulate reaction kinetics, an axially symmetric 2D model was constructed in ANSYS Fluent using user-defined functions (UDF) written in C++. The effects of radiation models (P-1, Rossland, and discrete ordinates (DO)), temperature, pressure, steam-to-carbon ratio (S/C), and gas hourly space velocity (GHSV) were studied. Among the radiation models, the DO model is the best matched with experimental data, showing superior heat transfer prediction. The results demonstrated that increasing reforming temperature and S/C ratio significantly enhance methane conversion, while GHSV had minimal influence. The highest methane conversion ratio of 98.15% was achieved under optimized conditions: 1073 K, 5 bar gauge pressure, S/C = 5, and GHSV = 5000 h^{-1}.

Building on this platform, the present work closes the process loop by coupling the reformer effluent to a condensate heat exchanger for controlled quench and to a fixed-bed CO_2 adsorber for H_2 purification. The integrated CFD-UDF framework transfers the SMR outlet state (T, P, m, yi) directly to a Toth/Sips-LDF adsorption model, enabling end-to-end evaluation of H_2 purity, recovery, and CO_2 capture and revealing the operating window that maximizes bed life and capture efficiency. Although many studies have investigated CO_2 capture and H_2 purification using PSA and fixed-layer adsorbents, most have focused on standalone adsorption systems or on optimizing PSA cycle configurations. Previous studies on SMR have mainly focused on increasing methane conversion and H_2 production within the reforming reactor itself. In contrast, the present work conducts an integrated CFD framework linking a previously validated SMR reactor with downstream gas cooling, water condensation, and fixed-bed CO_2 adsorption, allowing direct evaluation of how reformer operating conditions influence subsequent adsorption performance and hydrogen purification. A comprehensive parametric investigation quantifies the effects of adsorption temperature, pressure, feed composition, and GHSVs on breakthrough behavior, adsorption capacity, and bed utilization, offering practical design guidelines for coupling hydrogen production and carbon capture processes in blue hydrogen systems.

2. Methodology

The integrated process and modeling methodology used in this research are illustrated in Figure 1. Control valves are used to measure H_2O and CH_4 before they are combined in the gas mixer to adjust the S/C ratio. After the mixture is heated to the reformer inlet temperature in a preheater, it is fed through a tubular SMR reactor (which uses a nickel-based catalyst) to produce hot synthetic gas containing CO, CO_2, H_2, residual CH_4, and H_2O. To convert CO vapor into more CO_2 and H_2, the effluent can be directed to a WGS unit. The converted gas is cooled in a condensate heat

exchanger to the required adsorption inlet conditions; the water is then extracted. A fixed-layer adsorption column (an activated carbon adsorbent) is fed with the conditioned stream (a CO_2/H_2 mixture at the adsorption conditions). CO_2 is preferentially collected during adsorption, while hydrogen flows out. The bed is then regenerated in a dedicated desorber for the activation process. Valves and simple controllers enforce the sequence and hold the key setpoints: (T_{ads}, P_{ads}, CO_2/H_2 ratio, and GHSV).

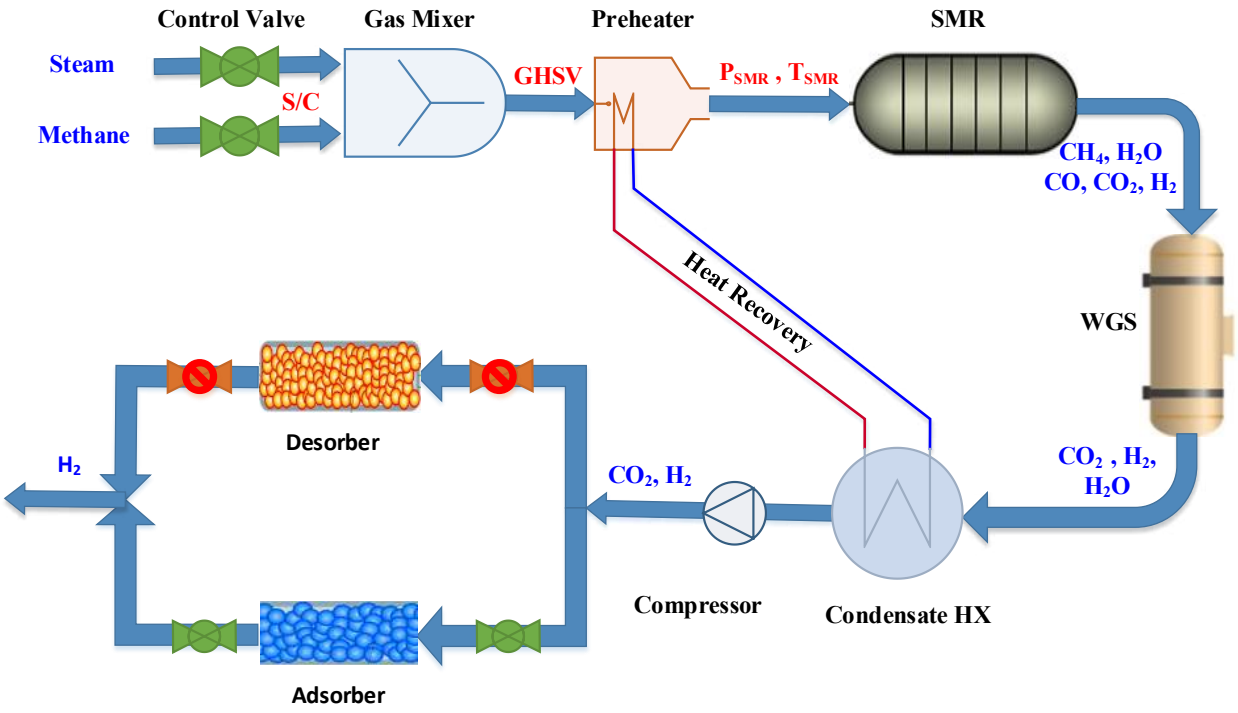


Figure 1 Schematic of the integrated SMR adsorption system for hydrogen purification

The units are numerically linked in sequence: after the heat exchanger unit set is defined, the SMR/WGS outlet state vector (temperature, pressure, gas volumetric flow ratio, mole fraction) serves as the entry boundary for the adsorption model. The adsorption layer is solved using an axially symmetric, 2D CFD model in ANSYS Fluent, employing UDF to integrate Toth and Sipes isotherms with UDF kinetics, porous medium flow resistance, and energy effects (heat of adsorption). Performance is reported locally (breakthrough curves, loads) and comprehensively (H_2 purity/recovery, CO_2 capture) under systematic adjustments for temperature (298-448 K), pressure (0-20 bar), CO_2/H_2 ratio (25/75, 50/50, and 75/25), and GHSV (100-500 h^{-1}).

3. Numerical modeling methods

3.1 Adsorber reactor and adsorbent specifications

In this study, a double-adsorber tube was used for numerical simulations, with one bed for the adsorption process and another for the activation process. The tube is axisymmetric, and the

governing equations and adsorption model were solved in a 2-D domain, as indicated in Figure 2. The adsorber is made of steel, is 20 cm long, and has a diameter of 0.91 cm. It is filled with an activated carbon adsorbent that has a porosity of 0.52 and particles with a diameter of 3.0 mm. CO_2 and H_2 are fed into the reactor tube through the feed inlet section. They pass through the porous adsorbent material (activated carbon) to adsorb CO_2. The specifications of the adsorber and adsorbent material are shown in Table 1.

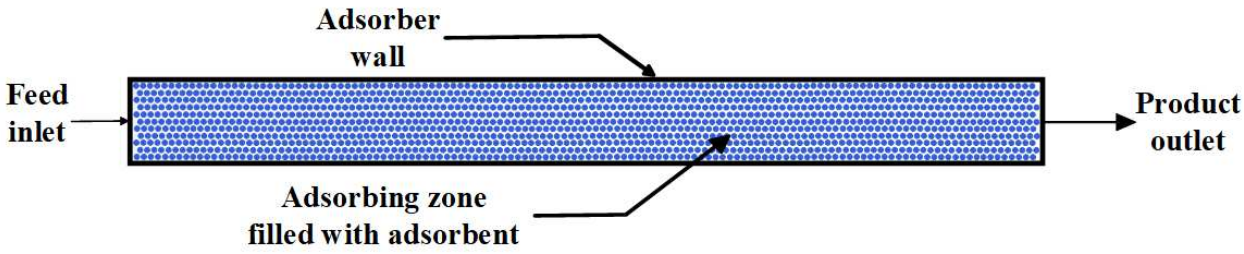


Figure 2 Axisymmetric schematic of the fixed-bed adsorption column.

Table 1. Adsorber and adsorbent material specifications.

Adsorber metal	*Steel*	Adsorbent material	*Activated carbon*
Adsorber length (cm)	*20*	Adsorbent porosity	*0.52*
Adsorber diameter (cm)	*0.91*	Adsorbent diameter (mm)	*0.3*
Adsorber thickness (cm)	0.1	Adsorbent density (kg/m^3)	850
Adsorber density (kg/m^3)	7800	Adsorbent heat capacity (J/kg K)	1000
Adsorber specific heat (J/kg K)	620.48	Adsorbent specific surface area (m^2/m^3)	8.5x10^8
Adsorber thermal conductivity (W/m K)	20	Adsorbent thermal conductivity (W/m K)	0.63

3.2 Governing equations

The governing equations for the transfer of mass, momentum, energy, and species are given in the following formulas [39], [40].

Continuity equation

$$\frac{\partial(\rho)}{\partial \mathrm{t}} + \nabla.(\rho\vec{v}) = (1-\varepsilon)\rho_p \sum_i M_i \frac{\partial q_i}{\partial \mathrm{t}} \quad (4)$$

Where: ρ (kg/m^3) is the gas density, $\vec{v}$ (m/s) is the velocity vector, ε is the bed porosity, M_i (kg/mol) is the molecular weight of species i (CO_2 and H_2), q_i (mmol/g) is the adsorbent amount of component i, and t (s) is the time.

Momentum equation

$$\frac{\partial(\rho\vec{v})}{\partial \mathrm{t}} + \nabla.(\rho\vec{v}\,\vec{v}) = -\nabla P + \nabla.\bar{\bar{t}} + \rho\,\vec{g} + S_i \quad (5)$$

where P (Pa) is the operating pressure, $\bar{\bar{t}}$ (N/m^2) is the stress tensor, $\vec{g}$ (m/s^2) is the gravity acceleration vector, and S_i (N/m^3) is the momentum source term in the porous media, which is calculated from the Ergun equation, including inertia and viscous resistances as (Xiao et al. [41]):

Source term

$$S_i = -\left(\frac{\mu}{K}\, v_i + C_2 \frac{1}{2}\, \rho\, |\vec{v}|\, v_i\right) \quad (6)$$

where μ (Pa.s) is the gas dynamic viscosity, 1/K ($1/m^2$) is the porous media viscous resistance, C_2 (1/m) is the inertial resistance, which has been computed using the Ergun equation [41]. Eqs. (7) and (8). $|\vec{v}|$ is the value of the velocity vector, and v_i is the velocity component in the i-direction.

Inertial resistance

$$\boldsymbol{C_2 = 3.5\ \frac{(1-\varepsilon)}{\varepsilon^3\ d_p}} \tag{7}$$

Viscous resistance

$$\boldsymbol{\frac{1}{K} = 150\ \frac{(1-\varepsilon)^2}{\varepsilon^3\ d_p^2}} \tag{8}$$

Energy equation

$$\frac{\partial}{\partial t}\left[\varepsilon\rho E_g + (1-\varepsilon)\rho_p E_s\right] + \nabla.\left[\left(\rho_p E_s + P\right)\right] = \nabla.\left[\boldsymbol{k_{eff}\ \nabla T} - \sum_i \boldsymbol{h_i\ \vec{J_i}} + \bar{\bar{\boldsymbol{t}}}.\vec{\boldsymbol{v}}\right] = \boldsymbol{(1-\varepsilon)\rho_p \sum_i \Delta H_i\ \frac{\partial q_i}{\partial t}} \tag{9}$$

Where E_g (J/m^3) is the total gas energy, E_s (J/m^3) is the total adsorbent energy, ΔH_i (J/ mol) is the heat of adsorption, which is different from one material to another and sometimes also varies with variation of gas adsorbed amounts, T (K) is the equilibrium temperature, h_i (J/kg) is the sensible enthalpy $h = \sum_i y_i h_i$, and J_i (kg/m^2 s) is the diffusion flux of the gas component i. The parameter k_{eff} is the effective conductivity of the adsorbent bed and can be expressed as (Ansys fluent [39]; Xiao et al. [41]); Mansour et al. [42]:

$$k_{eff} = \varepsilon\, k_g + (1-\varepsilon)\, k_s \tag{10}$$

where k_g and k_s (W /m K) are the thermal conductivities of the gas mixture and adsorbent, respectively.

Species equation

$$\nabla.\left(\varepsilon\rho_g \vec{u}\, Y_j\right) = \nabla.\left(\rho_g D_j.\nabla Y_j\right) + (1-\varepsilon)\rho_c\, M_j \sum_{i=1}^{n} r_i v_{i,j} \tag{11}$$

Where Y_j (kg_j/kg_{mix}) is the mass fraction of the species, D_j (m^2/s) is the diffusion coefficient for the species, and r_i ($kg_j/m^3 s$) is the source or sink term.

The temperature change in the wall is determined by a balance between the rate of internal energy storage and the rate of conductive heat transfer through the material:

$$\frac{\partial}{\partial t}(\rho_w C_w T_w) = \nabla\,(k_w\,\nabla T_w) \tag{12}$$

Where, ρ_w (kg/m^3) is the wall density, C_w (J/kg K) is the wall heat capacity, T_w (K) is the local temperature of the wall, and k_w (W/m K) is the thermal conductivity of the wall material.

The exchanger performance directly influences adsorption efficiency by controlling temperature, pressure, and feed gas composition. The energy balance (steady state, no shaft work) can be represented as the heat removed from the hot stream or heat gained by the coolant (neglected losses):

Energy balance $$\dot{Q} = \dot{H}_{hot,in} - \dot{H}_{hot,out} = \dot{H}_{cold,out} - \dot{H}_{cold,in} \quad (13)$$

$$\text{Where } \dot{H} = \dot{n}\,\bar{h}(\text{T, P}) \quad (14)$$

LMTD method $$\dot{Q} = UA\Delta T_{Lm} \quad (15)$$

$$\text{Where } \Delta T_{Lm} = \frac{\Delta T_{max} - \Delta T_{min}}{Ln(\Delta T_{max}/\Delta T_{min})} \quad (16)$$

3.3 Adsorption Isotherm and Kinetics Models

The adsorption isotherms used in this work are described with a Toth isotherm [43] and Sips isotherm [44], [45] for the adsorption of CO_2 and H_2, respectively, on activated carbon. The Toth isothermal model, used to describe the adsorption of carbon dioxide onto activated carbon, is particularly effective in monitoring adsorption behavior on heterogeneous surfaces. It is expressed as [43]:

Toth model $$q_i^* = q_{i,max}\,\frac{k_{i,eq}y_iP}{\left[1 + (k_{i,eq}y_iP)^n\right]^{1/n}} \quad (17)$$

Where q_i^* (mol/kg) is the equilibrium adsorbed amount of component i, $q_{i,max}$ (mol/kg) is the maximum adsorption capacity, $k_{i,eq}$ (bar^{-1}) is the affinity constant reflecting adsorption strength, y_i is the gas-phase mole fraction, P (bar) is the total pressure, and n is the dimensionless Toth exponent quantifying surface heterogeneity (with n=1 reducing the model to the Langmuir isotherm. This model is particularly effective for the adsorption of CO_2 on porous materials like activated carbon, capturing deviations from ideality due to energy.

The Sips isotherm provides a more reliable model at moderate to high pressures by combining the Langmuir and Freundlich approaches [44].

Sips model $$q_i^* = q_{i,max}\,\frac{(k_{i,eq}y_iP)^{n_s}}{1 + (k_{i,eq}y_iP)^{n_s}} \quad (18)$$

Where, n_s is the dimensionless Sips exponent. Both models are essential for designing adsorption-based separation systems, with the Toth isotherm excelling in CO_2 applications due to its sensitivity to surface energy variations, and the Sips isotherm offering flexibility for H_2 adsorption across diverse pressure ranges.

The rate of change in the adsorbed is described by the Linear Driving Force (LDF) model [46]:

LDF model $$\frac{\partial q_i}{\partial t} = k_{L,i}(q_i^* - q_i) \quad (19)$$

Where: q_i^* is the equilibrium concentration determined from the Toth or Sips isotherm, q_i (mmol/g) presents the actual adsorbed amount, and $k_{L,i}$ is the lumped mass transfer coefficient (s^{-1}). $k_{L,i}$ is estimated by considering the combined resistances of the gas film, macropores, and micropores

that gases encounter when passing through porous materials. The relationship is given by the equation:

Mass transfer Coeff.
$$\frac{1}{k_{L,i}} = \frac{r_p q_{0,i}}{3\, k_{f,i} C_{0,i}} + \frac{{r_p}^2\, q_{0,i}}{15\, \boldsymbol{\varepsilon}_p\, D_{p,i}\, C_{0,i}} + \frac{{r_C}^2}{15\, D_{C,i}} \quad (20)$$

The terms $q_{0,i}$ and $C_{0,i}$ (mol/m³) represent the equilibrium concentrations in the solid and gas phases, respectively. The adsorbent particle radius is denoted by r_C (m), its porosity by $\boldsymbol{\varepsilon}_p$, and the adsorbent crystal radius by r_C. The mass transfer coefficients $k_{f,i}$ (film), $D_{p,i}$ (macroporous diffusion), and $D_{C,i}$i (microporous diffusion) for each component i are evaluated according to the methods established by Dantas et al. [46] and He et al. [47].

According to the LDF model, the difference between the equilibrium value and the amount of adsorbed material directly determines the adsorption rate. This method maintains the accuracy of dynamic simulations, such as penetration curves and cyclic operation, while simplifying the modeling of intraparticle diffusion. The significantly higher adsorption affinity of CO_2 compared with H_2 on activated carbon originates from the stronger intermolecular interactions between CO_2 molecules and the carbon surface. Carbon dioxide has a substantially higher critical temperature, polarizability, and quadrupole moment than hydrogen, leading to stronger van der Waals interactions and greater adsorption capacity under identical operating conditions. In contrast, hydrogen exhibits very weak physisorption at near-ambient temperatures and moderate pressures. Consequently, CO_2 is preferentially retained within the porous adsorbent while H_2 rapidly passes through the bed, enabling effective gas separation and hydrogen purification.

3.4 Boundary Conditions

- *External Wall Boundary Condition*

The boundary conditions at the outer wall of the adsorption column in this study account for both conventional and radiation heat transfer to the surroundings. The heat flux through the wall is described by the following equation:

$$k_w \left(\frac{\partial T_w}{\partial n}\right)_w = h_{ext}(T_w - T_{amb}) + \varepsilon_w\, \sigma({T_w}^4 - {T_{amb}}^4) \quad (21)$$

where k_w is the wall thermal conductivity (W/m K), T_w is the wall temperature (K), T_{amb} is the ambient temperature (K), h_{ext} is the external convective heat-transfer coefficient (W/m^{2}K), the ε_w is the wall surface emissivity (-), σ is the Stefan-Boltzmann constant (5.67 x 10^{-8} W/m^{2}K), and $(\partial T_w/\partial n)_w$ is the temperature gradient normal to the wall surface.

The external convective heat transfer coefficient, h_{ext}, is obtained from a Nusselt-number correlation [48] appropriate for natural convection around a cylindrical wall:

$$Nu_w = \frac{h_{ext} d_o}{k_{air}} = \left[0.6 + \frac{0.387\, Ra^{1/6}}{\left(1 + \left(\frac{0.559}{Pr_{air}}\right)^{9/16}\right)^{8/27}} \right]^2 \quad (22)$$

where d_0 (m) is the external diameter of the wall, k_{air} (W/m K) is the thermal conductivity of air evaluated at the film (average) temperature ($T_f = (T_w + T_{amb})/2$), Pr_{air} is the air Prandtl number, and Ra is the Rayleigh number (also evaluated at T_f).

For adiabatic walls $$\left(\frac{\partial T_w}{\partial n}\right)_w = 0 \quad (23)$$

- *Inlet boundary conditions*

At the inlet of the adsorption bed, the boundary conditions are specified by balancing the diffusive transport with the convective transport of mass and energy between the incoming feed stream and the first computational cell inside the bed. Accordingly, the following relations are applied for each species i and for energy:

$$-\varepsilon D_{i,m} \nabla y_i = \vec{v}\,(y_i|_- - y_i|_+) \quad (24)$$

$$-\varepsilon k_{eff} \nabla T = \vec{v}\,\rho\,(h_i|_- - h_i|_+) \quad (25)$$

Where ε is the bed porosity, $D_{i,m}$ the effective mass diffusivity of species i, k_{eff} the effective thermal conductivity, $\vec{v}$ the superficial inlet velocity, $y_i|_-$ and $h_i|_-$ the feed mass (or mole) fraction and specific enthalpy, and $y_i|_+$ and $h_i|_+$ the corresponding values are just inside the bed.

- *Outlet boundary conditions*

The mass and heat fluxes at the axisymmetric axis and at the exit can be expressed as follows:

$$\nabla y_i = 0 \quad (26)$$

$$\nabla T = 0 \quad (27)$$

- *Interfaces between walls and adsorbent*

For the 2D model, heat transfer at the bed-wall interface is evaluated based on the temperature difference between the wall and the adjacent adsorbent. The heat exchange is characterized by the internal convective heat transfer coefficient, h_i, and is linked to the local conductive heat transfer within the packed bed.

$$k_{eff} \left(\frac{\partial T}{\partial n}\right)_w = h_i\,(T - T_w) = k_{local} \left(\frac{\partial T}{\partial n}\right)_{local} \quad (28)$$

3.5 CFD modeling and assumptions

In this study, 2D-CFD modeling has been used to investigate the adsorption process. ANSYS Fluent 2025-R2 was utilized for the model after being coupled with a UDF code developed in C++ language, where UDF were combined to implement the Toth and Sips models for the adsorption of CO_2 and H_2, respectively. The governing equations were formulated with appropriate initial and boundary conditions described in Section 3, including temperature (ranging from 298 to 484 K), pressure (gauge pressure 0-20 bar), CO_2/H_2 molar ratio (25/75-75/25%), and GHSV (100-500 h^{-1}). Pressure-velocity coupling was addressed using the Semi-Implicit Method for Pressure-Linked Equations (SIMPLE). The load limits in the momentum, energy, and species transfer equations were approximated using a first-order inverse variance scheme. Convergence criteria of 10^{-5} were established. To ensure numerical accuracy and stability, the continuity, momentum, species, and energy equations were defined. A transient analyzer was used to monitor the time-varying adsorption behavior, including penetration and layer saturation phenomena, enabling realistic simulations of gas separation processes and their performance under varying operating conditions. To streamline the model and cut down on computation time, several assumptions were considered; a list of them is provided below:

- Laminar flow in transient flow, wall radiation, and convection situations have been examined.
- The feed inlet of the adsorber consists of pure CO_2 and H_2, and the gas mixtures are assumed to be in an ideal gas state.
- The inertial and viscous resistances are the same in all directions, and the reformer catalytic bed has been described as pseudo-homogeneous.
- Mass, heat, and velocity gradients are considered in axial and radial directions.

A limiting condition for the inlet velocity and a limiting condition for the outlet pressure were applied at the inlet and outlet of the adsorption bed, respectively, throughout the reforming process. The mixture applied to the fixed outer wall of the adsorption device was assumed to enter the bed at the same constant temperature as the inlet of the adsorption zone.

4. Mesh and Time-Step Independence and Model Validation

4.1 Mesh independence

For the axisymmetric geometry, a structured quadrilateral mesh was chosen over unstructured triangular meshes due to its superior orthogonality and excellent solution accuracy. As shown in Figure 3, this mesh technique also allows fewer elements while preserving numerical stability and convergence, particularly near the wall.

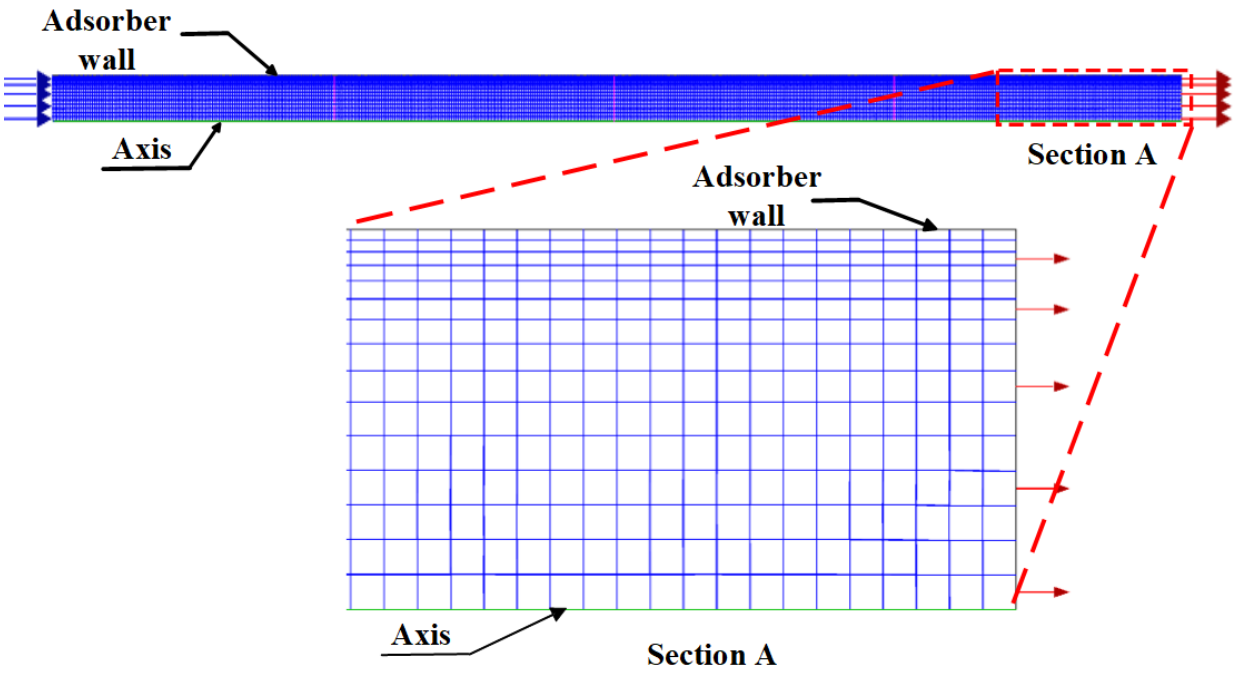


Figure 3. 2D Mesh configuration of the adsorber bed.

To ensure numerical accuracy and network-independent results, network sensitivity analysis was performed using four structured networks with 160, 1000, 2000, and 10005 cells, respectively. The corresponding network quality metrics showed the lowest orthogonality quality of 1 and the highest aspect ratios of 6.75, 3.66, 3.25, and 3.05, respectively. The analysis was performed under constant operating conditions of 298 K, 0 bar gauge pressure, a 50/50 CO_2/H_2 molar ratio, and a GHSV of 100 h^{-1}, with the molar fractions of CO_2 and H_2 at the outlet chosen as the evaluation criteria. As shown in Figure 4, the predicted outlet configurations showed little variation for networks containing 1000 or more cells, indicating network-independent behavior. Therefore, the 1000-cell grid was adopted for all subsequent simulations, providing a suitable balance between computational cost and solution accuracy.

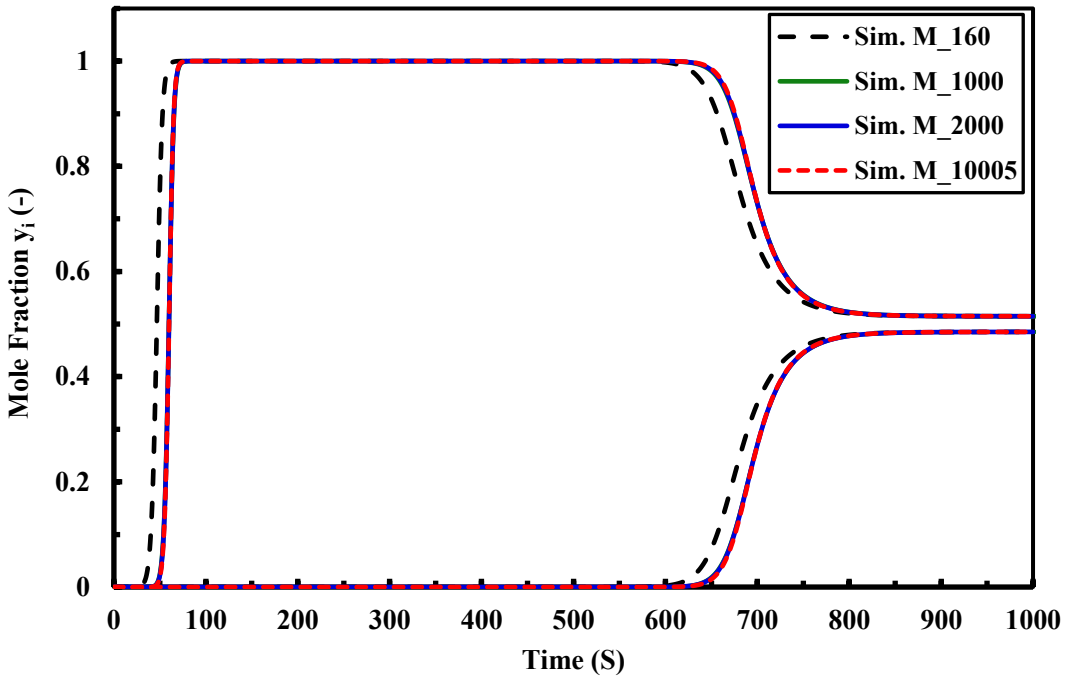


Figure 4 Mesh independence study for different cell numbers

4.2 Time-Step Independence

The independence of the time step was investigated by varying the time step (Δt) and monitoring its effect on the predicted molar fractions of CO2 and H2 at the reactor outlet to ensure the accuracy and stability of the transition simulation results. Four different time steps-0.1, 1.0, 5.0, and 60.0 seconds-were evaluated under continuous operating conditions at 298 K, 0-gauge bar, a 50/50 mol% of CO_2/H_2 ratio, and GHSV of 100 h^{-1}. As shown in Figure 5, the mole fractions of CO_2 and H_2 at the outlet converge at time intervals of 0.1 s, 1.0 s, and 5.0 s, with slight deviations between the results. However, the penetration time and final equilibrium values are inaccurate in simulations with an estimated time step of 60 seconds, due to significant numerical variability and a delay in predicting the adsorption front. This pattern suggests that very long time steps may impair the model's ability to capture rapid changes in species and temperature accurately. Based on this analysis, a time step of 1.0 seconds was chosen for all subsequent transient simulations. For long-term simulations, this value maintains reasonable computational costs while ensuring stability and numerical accuracy.

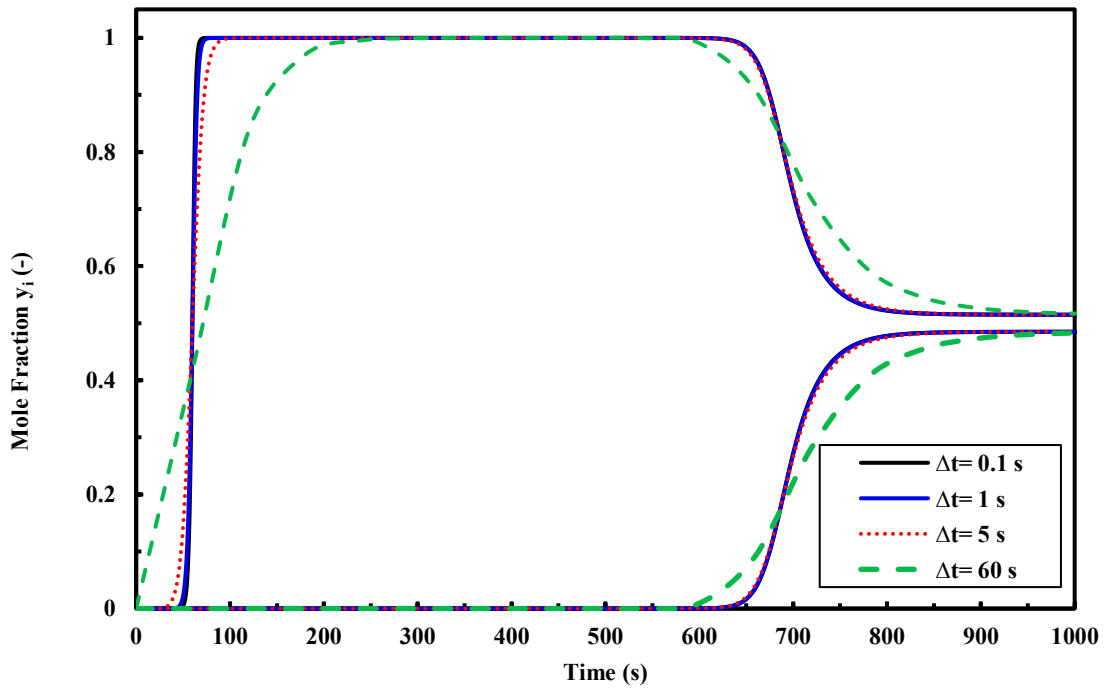


Figure 5. Time-step independence study

4.3 Validation against CO_2/H_2 over activated carbon Sips Model - Casas et al.[49]

A comparison was made using experimental penetration data from Casas et al. [49]to validate H2 breakthrough in a H_2-CO_2 mixture. CO_2/H_2 separation in a fixed-bed adsorption system packed with activated carbon was investigated as shown in Figure 6. The reference case selected for validation involved a 50/50 mol% CO_2/H_2 gas mixture, operated at 15 bar and 25 °C, with a feed flow rate of 10 cm^3/s. In the simulation, the same operating parameters and Sips-based isotherm formulations were employed to replicate the breakthrough behavior of hydrogen. The simulated H_2 breakthrough curve was then compared with the experimental data reported by Casas et al. [49], using the thermal and adsorption properties as described in Table 2.

Table 2. Thermal and adsorption properties of CO_2/H_2 over activated carbon, Casas et al [49].

Parameter	Value	Unit	Parameter	Value	Unit
length	1.2	m	Bed Porosity	0.403	-
Radius	0.0125	m	Total porosity	0.742	-
Pressure	15	bar	Temperature	298	K
Flowrate	10	cm^3/s	CO_2/H_2 ratio	50/50	%
AC Density	850	Kg/m^3	AC diameter	0.003	m
Specific surface area	$8.5x10^8$	m^2/m^3	Solid heat capacity	1000	J/(kg·K)
h	5	W/m^2 K	Molecular Diffusion	$4.3x10^{-6}$	m^2/s
σ	5.67×10^{-8}	W/m^2K	ε_w (emissivity)	0.8	-
ΔH_{CO_2}	−26000	J/mol	ΔH_{H_2}	-9800	J/mol
k_{CO_2}	0.15	s^{-1}	K_{H_2}	1.0	s^{-1}

This verification confirms that the kinetic models, heat adsorption diagrams, and governing equations used in this study are suitable for modeling H_2/CO_2 separation in activated carbon layers under PSA-related conditions. As shown in Figure 6, the model accurately captures the early breakthrough behavior of H_2, including the timing and shape of the breakthrough curve, reflecting the weak adsorption of hydrogen on activated carbon. Although there are slight variations in the later stages of breakthrough, likely due to uncertainties in layer filling and the properties of the adsorbent material, the simulation mimics the delayed penetration and gradual saturation of the layer experimentally observed for CO_2. Overall, the model provides a reliable representation of the adsorption dynamics, with RMSE values of 0.0634 for H_2 and 0.0590 for CO_2, confirming good agreement with the experimental data of Casas et al. [49].

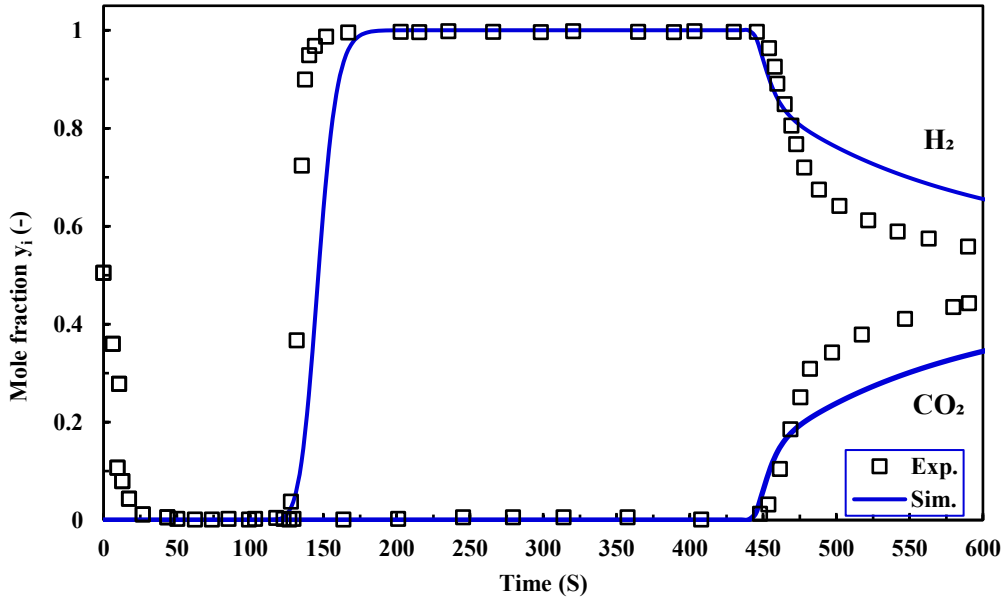


Figure 6 Validation of the CO_2/H_2 adsorption process with experimental data of Casas et al. [49]

4.4 Validation against CO_2/N_2 over activated carbon Toth model - Dantas et al. [46]

To further verify the accuracy of the developed numerical model, a validation study was conducted by comparing simulation results with the experimental data of Dantas et al. [46] for a CO_2/N_2 mixture under constant adsorption. With a focus on carbon dioxide capture after combustion, researchers investigated the separation of CO_2 from N_2 using adsorption in a stable layer on commercially available activated carbon. Innovative experiments were conducted using carbon dioxide/nitrogen mixtures at various temperatures (301-423 K), and the Toth thermal model was employed to study the adsorption behavior. The LDF model, which incorporated momentum and

energy balances, accurately predicted the adsorption dynamics. The operating conditions of the validated test were 423 K, 0- gauge bar, and a CO_2/N_2 ratio of 20/80 mol% as shown in Table 3.

Table 3. Thermal and adsorption properties of CO_2/H_2 over activated carbon, Dantas et al. [46]

Parameter	Value	Unit	Parameter	Value	Unit
length	0.171	m	Adsorbent particle size	0.0038	m
Radius	0.011	m	Inlet velocity	0.00131	m/s
Bed wall thickness	0.0015	m	Inlet temperature	423	K
Bed density	546.24	kg/m^3	Ambient temperature	298	K
Particle density	1138	kg/m^3	Outlet pressure	0	bar
Bed porosity	0.52	-	CO_2/N_2 ratio	20/80	%
Adsorbent specific heat capacity	880	J/kg K	Adsorbent thermal conductivity	0.63	W/m K
ΔH_{CO2}	−21840	J/mol	ΔH_{N2}	−16310	J/mol

The concentration ratio (C/C_0) at the bed outlet was used to plot the breakthrough curves. The simulated and experimental CO_2 adsorption curves using the Toth model showed good agreement, as shown in Figure 7. However, slight variations were found for N_2 in the initial breakthrough region, which are likely due to filler heterogeneity or uncertainties in the material properties. The model successfully captured the overall adsorption behavior and CO_2 saturation dynamics, with RMSE values of 0.0895 for N_2 and 0.051 for CO_2, confirming good predictive accuracy, particularly for the primary adsorbing species, CO_2.

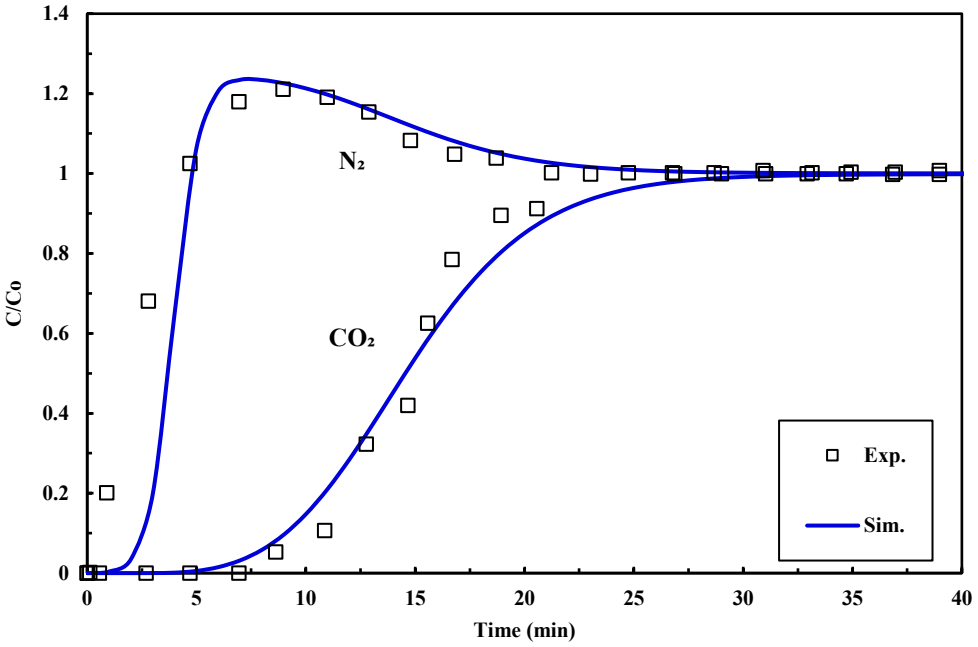


Figure 7 Validation of the CO_2/N_2 adsorption process with experimental data of Dantas et al. [46].

Overall, both validation cases CO_2/H_2 separation using the Sips model as Casas et al. [49] and CO_2/N_2 separation using the Toth model as Dantas et al. [46], demonstrated that the numerical

model can capture the essential dynamics of multicomponent gas adsorption in activated carbon beds. Although there were slight variations in the final breakthrough stage, the simulation using the Sips model reasonably represented CO_2 behavior and showed high agreement with experimental H_2 adsorption data. In contrast, the Toth model's predictions for N_2 were less accurate, particularly in the early stages of adsorption, but still provided very strong agreement with experimental evidence for CO_2 in the CO_2/N_2 state. Given its high efficiency in monitoring H_2 dynamics and its adaptability to modeling heterogeneous surfaces under high pressure, these results suggest that the Sips model is better suited for simulating competitive adsorption involving H_2. Therefore, the Sips isotherm model is recommended for use in this study, particularly for purification of H_2 and capture of CO_2 scenarios involving pre-combustion gas mixtures. The adopted UDF model is based on previous experimental and modeling work, including the studies by Dantas et al. [46] on CO_2/N_2 adsorption and by Casas et al. [49] on CO_2/H_2 mixtures.

5. Results and discussions

In our previous study [38], the performance of an SMR was optimized by investigating the effects of operating pressure, temperature, S/C, and GHSV. The results showed that low pressure, high temperature, and a high S/C ratio provide optimal conditions for methane reforming, consistent with the thermodynamics of endothermic reactions and the inhibition of carbon deposition by excess steam. The highest methane conversion rate of 98.15% was achieved at a pressure of 5 bar, a temperature of 1073 K, an S/C ratio of 5, and a GHSV of 5000 h^{-1}. Under these conditions, the reformer's outlet current was very hydrogen-rich, with molar ratios of: $H_2 = 0.482$, $H_2O = 0.420$, $CO_2 = 0.084$, $CO = 0.019$, and $CH_4 = 0.003$. These operating conditions combine favorable reaction kinetics, enhanced equilibrium, and vapor mitigation effects, resulting in high CH_4 conversion with reduced residual CH_4 and CO. Because CO and CH_4 are already very small, they can often be neglected in the downstream separation design. Moreover, routing the gas through a WGS reactor and then a condensate heat exchanger removes most steam and shifts CO to H_2 and CO_2; the resulting dry reformate fed to adsorption is therefore dominated by H_2 (85 mol%) with CO_2 (15 mol%), which is the working composition used in the capture step as shown in Table 4.

Table 4. Integrated SMR, WGS, HX, and Adsorber stream summary (conditions and compositions)

Stream	Operating Conditions		Mole Fraction %					Note
	T(K)	P (bar)	H_2O	CH_4	CO	H_2	CO_2	
SMR out	1073	5.0	41.2	0.3	1.9	48.2	8.4	SMR best case; CH_4 conv. 98.15%
WGS out	673	5.0	42.2	≈ 0.0	≈ 0.0	49.3	8.5	CO→CO_2; wet basis
HX out	298	5.0	0.0	≈ 0.0	≈ 0.0	85	15	Cooling and steam condensation
Compressor out	298	20.0	0.0	≈ 0.0	≈ 0.0	85	15	Pressurization
Adsorber in	298	20.0	0.0	≈ 0.0	≈ 0.0	85	15	Dry basis (85/15 H_2/CO_2)
Adsorber out	298	20.0	0.0	0.0	0.0	>99.9	0.0	H_2 product purity

The stream is hydrogen-rich, with some H_2O and CO_2, and only trace amounts of CH_4 and CO (indicating 98.15% CH_4 conversion) starting from the outlet of the SMR unit (1073 K, 5 bar). Most of the CO is converted to CO_2 by the WGS stage under the same conditions, with a slight increase in the wet-weight hydrogen content. To remove the water and provide an 85/15 dry supply of H_2 and CO_2 for adsorption, a downstream heat exchanger cools the gas to 298 K and raises it to 20 bar. Under these conditions, the adsorbent provides 100% hydrogen (dry weight), indicating complete CO_2 capture.

Figure 8A illustrates the axial SMR directions that produce this composition: the CH_4 decreases near the inlet, the concentration of H_2 increases to 0.85, then the vapor concentration decreases, and the CO_2 concentration increases to 0.15. Figure 8B illustrates the adsorption outlet response: a long initial period of 100% hydrogen concentration ($CO_2 = 0$), followed by a desorption phase, where the H_2 concentration decreases, and the CO_2 concentration increases to feed values with the adsorption layer becoming saturated.

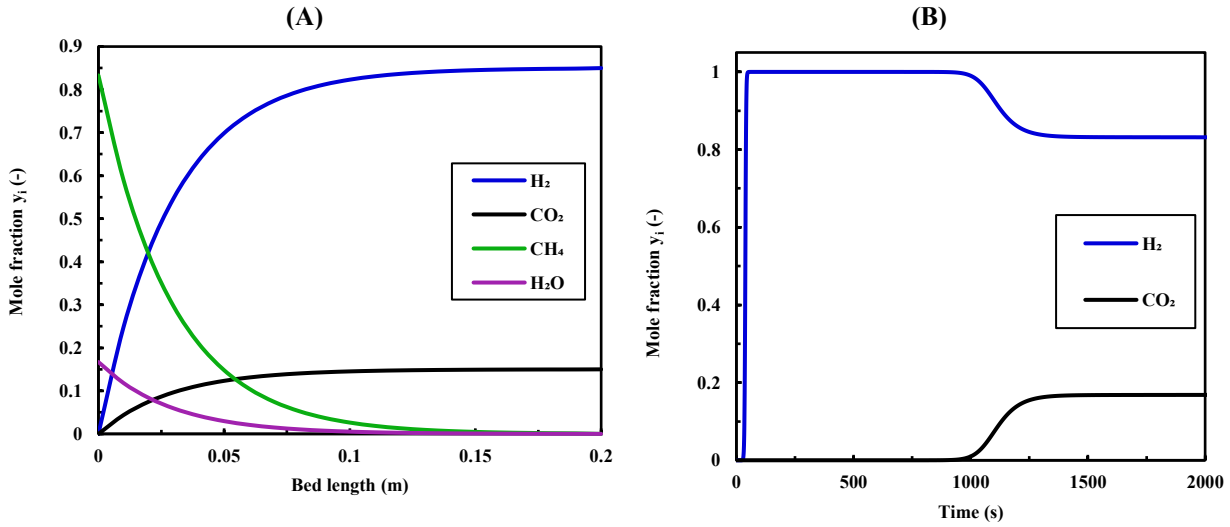


Figure 8 Integrated SMR-adsorption system: (A) axial species mole-fraction profiles along the SMR; (B) time evolution of outlet mole fractions during the adsorption step.

This work examines how important operating factors affect the ability of a fixed-layer adsorption system to purify H_2 from CO_2 and H_2 mixtures. Several factors affect the adsorption process, bed saturation, and overall CO2 capture efficiency, including adsorption temperature, pressure, GHSV, and inlet gas composition (CO_2/H_2 ratio), as shown in Figure 9.



Figure 9 Parametric study matrix and operating conditions used for the adsorption simulations.

5.1 Effect of CO_2/H_2 adsorption temperature

Figure 10 illustrates the effect of adsorption temperature on the breakthrough behavior of CO_2 and H_2 in a fixed-bed adsorption system. Simulations were performed at four temperatures: 298, 348, 398, and 448 K, with all other operating parameters held constant as P=0 bar, GHSV=100 h^{-1}, and CO_2/H_2=50/50%. At the lowest temperature, 298 K, CO_2 remains in the bed for much longer before desorption, exhibiting strong adsorption and high retention capacity. In contrast, the H_2 breaks through almost instantaneously and dominates the outlet stream due to its weak interaction. As the

adsorption temperature increases, CO_2 begins to penetrate earlier, indicating a reduced sorbent capacity to retain CO_2. At the highest temperature, 448 K, both CO_2 and H_2 exit the bed almost simultaneously, indicating a significant decrease in adsorption efficiency. This behavior is expected because CO_2 adsorption is an exothermic process, and higher temperatures thermodynamically reduce the affinity between CO_2 and the adsorbent surface.

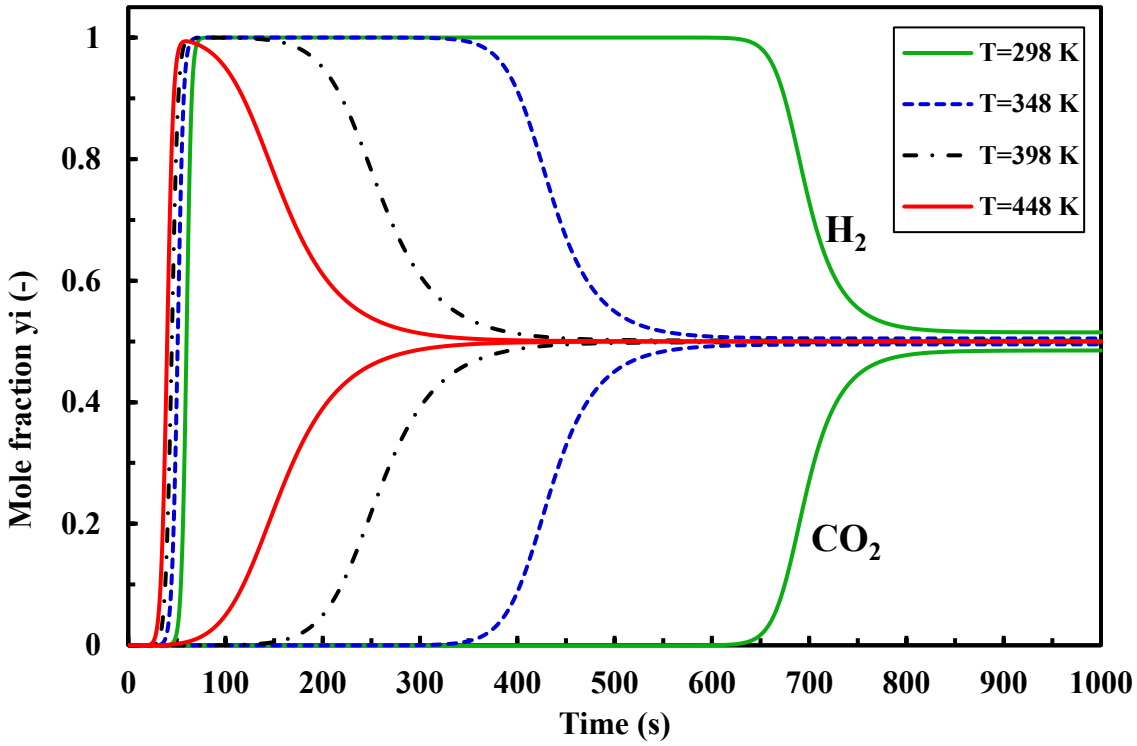


Figure 10. Effect of Adsorption Temperature on CO_2 and H_2 Breakthrough Curves.

The breakthrough curves of CO_2 and H_2 in Figure 10 do not converge at 298 K. This is because CO_2, unlike H_2, is adsorbed more intensely at this low temperature, resulting in delayed and incomplete adsorption. Since CO_2 is better retained by the adsorbent, its resulting concentration remains lower than that of hydrogen. On the other hand, because CO_2 adsorption is exothermic, it diminishes at higher temperatures (348 K and above), allowing carbon dioxide to penetrate more rapidly and reach the same resulting H_2 concentration. This causes the curves to converge, indicating that both gases exit the layer at similar rates as adsorption becomes less effective.

Figure 11 provides further details by showing the time-dependent changes in the amount of CO_2 adsorbed (q_{CO_2}) at the same four temperatures. The results show that decreasing temperatures facilitate the adsorption of larger quantities of CO_2. The adsorption capacity gradually increases, reaching its maximum value at 298 K. Both the adsorption rate and the final CO_2 load decrease significantly with increasing temperature. At 448 K, the amount of adsorbed CO_2 remains low and rapidly stabilizes, reflecting a decrease in the driving force for adsorption. This trend reinforces previous observations from the breakthrough curves and highlights the thermodynamic limitations

of CO_2 adsorption at high temperatures. Overall, the results clearly demonstrate that low adsorption temperatures significantly enhance the capacity and efficiency of CO_2 removal in hydrogen purification applications.

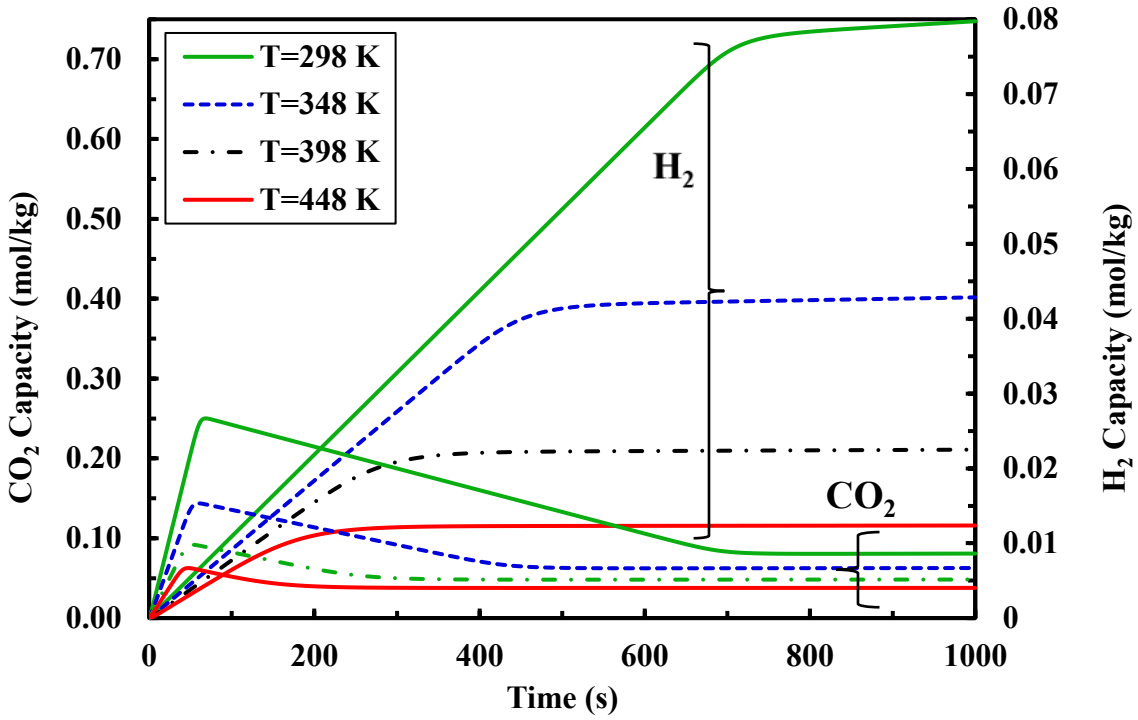


Figure 11. Effect of temperature on CO2 and H2 adsorption capacity.

5.2 Effect of CO_2/H_2 adsorption pressure

Figure 12 illustrates the effect of adsorption pressure on the breakthrough behavior of CO_2 and H_2 in a fixed-layer adsorption column. Simulations were performed at four different gauge pressures: 0, 5, 10, and 20 bar, while maintaining constant temperature, gas composition, and flow conditions (T=298 K, GHSV=100 h^{-1}, and CO_2/H_2=50/50%). Increasing the adsorption pressure significantly slows CO_2 penetration, as the graph illustrates, indicating greater adsorption capacity at higher pressures. At zero bar, H_2 escapes immediately due to its weak contact with the adsorbent, while CO_2enters the adsorption layer quickly and saturates it rapidly. As the pressure increases to 5 and 10 bar, the CO_2 penetration time shifts further to the right, indicating that the bed retains CO_2 for a longer period and more effectively. At the highest pressure of 20 bar, CO_2 is adsorbed for the longest period before any significant breakthrough occurs. High partial pressures increase the driving force of mass transfer, encouraging further CO_2 uptake, consistent with the positive pressure dependence of physical adsorption. This delays layer saturation and prolongs the period of decline in the molar fraction of CO_2 at the outlet. Meanwhile, H_2 continues to exhibit an early and sustained advance at all pressures, enhancing its limited adsorption capacity. These results confirm that operating at higher adsorption pressures improves CO_2 capture performance, making pressurized conditions suitable for hydrogen purification applications.

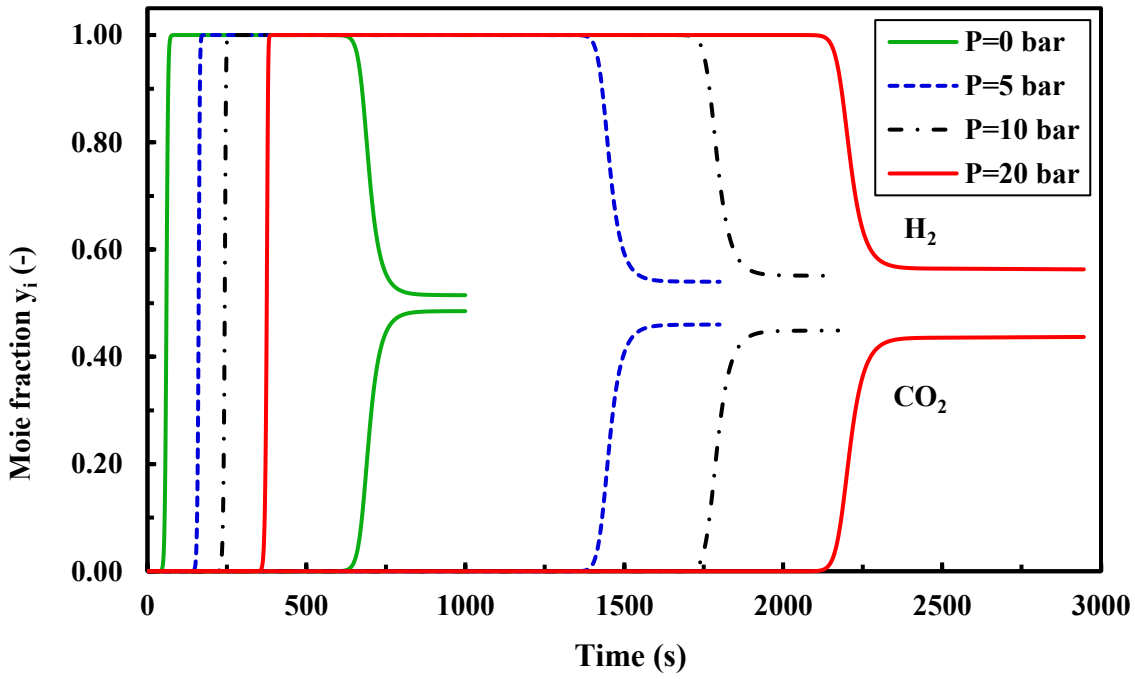


Figure 12. Effect of Adsorption Pressure on CO_2 and H_2 Breakthrough Curves.

In Figure 12, the divergence between the CO_2 and H_2 lines widens as the pressure increases. This is due to the adsorbent's enhanced ability to retain CO_2 at higher pressures, thus prolonging its stay in the layer. H_2, on the other hand, flows freely at any pressure because it is not adsorbed at all. The two gases behave differently with increasing pressure: CO_2 remains in the layer while H_2 continues to flow out, increasing the distance between their concentrations at the outlet. Higher pressure improves CO_2 adsorption while allowing hydrogen to flow more freely, which is beneficial for gas separation.

Figure 13 illustrates the effect of pressure on the amount of adsorbed CO_2 (q_{CO_2}) over time in the fixed-bed adsorption system. The results were plotted for four different measurement pressures (0, 5, 10, and 20 bar) while maintaining constant temperature and gas composition. The graph clearly shows that the adsorption capacity of CO_2 increases significantly with increasing pressure. Adsorption peaks at approximately 0.75 mol/kg at 0 bar, then stabilizes. The amount of CO_2 adsorbed gradually increases with pressure up to 5 bar, then 10 bar, and finally 20 bar, reaching over 2.4 mol kg^{-1} at 20 bar. This demonstrates that pressure increases the driving force for mass transfer, enabling greater adsorption of CO_2 onto the activated carbon.

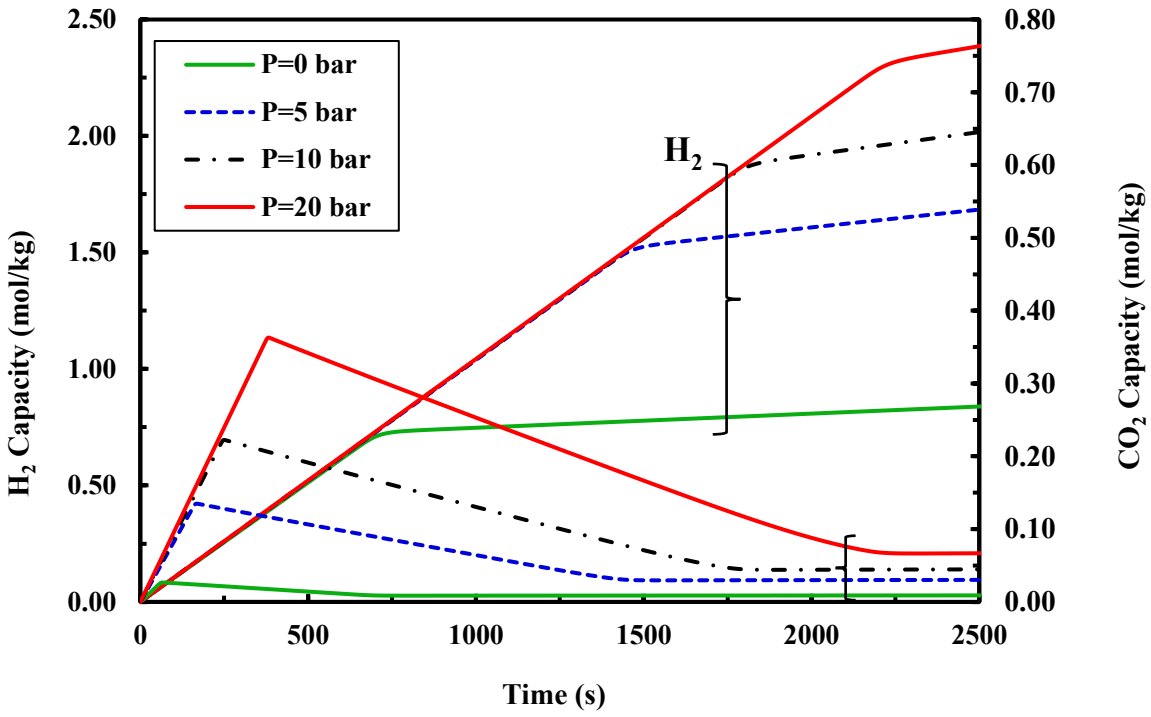


Figure 13. Effect of Pressure on CO_2 Adsorption Capacity Over Time

5.3 Effect of Feed H_2/CO_2 ratio

Figure 14 illustrates how varying the inlet CO_2/H_2 molar ratio influences the breakthrough behavior in a fixed-bed adsorption column. Three configurations (25/75, 50/50, and 75/25) were simulated under constant operating conditions of 0 bar gauge pressure, 298 K, and a GHSV of 100 h^{-1}. As shown in the figure, increasing the CO_2 concentration in the feedstock accelerates the CO_2 breakthrough time, resulting in faster saturation of the adsorption layer. At 25% CO_2 concentration, breakthrough occurs relatively late, and the adsorption layer retains CO_2 for a longer period, leading to higher adsorption efficiency. However, as the CO_2 content increases to 50% and 75%, the breakthrough front moves earlier, and the adsorption layer reaches saturation more rapidly due to the increased amount of CO_2 entering the column. This trend is attributed to the rapid saturation of available adsorption sites at high CO_2 concentrations, which limits the adsorption layer's ability to maintain effective separation over time. In addition, a high percentage of incoming CO_2 increases partial thrust but also leads to a faster depletion of the adsorbent material's capacity. This trend can be attributed to the rapid saturation of available adsorption sites at higher CO_2 concentrations, limiting the bed's ability to maintain effective separation over time. In addition, a higher inlet CO_2 ratio increases the partial pressure driving force but also exhausts the adsorbent capacity more quickly. Meanwhile, during the adsorption phase, H_2, which has weak adsorption, penetrates the surface layer early and controls the output current. Overall, the results show that lowering the CO_2 to H_2 ratio improves hydrogen purification performance by extending the surface layer lifetime and increasing CO_2 adsorption.

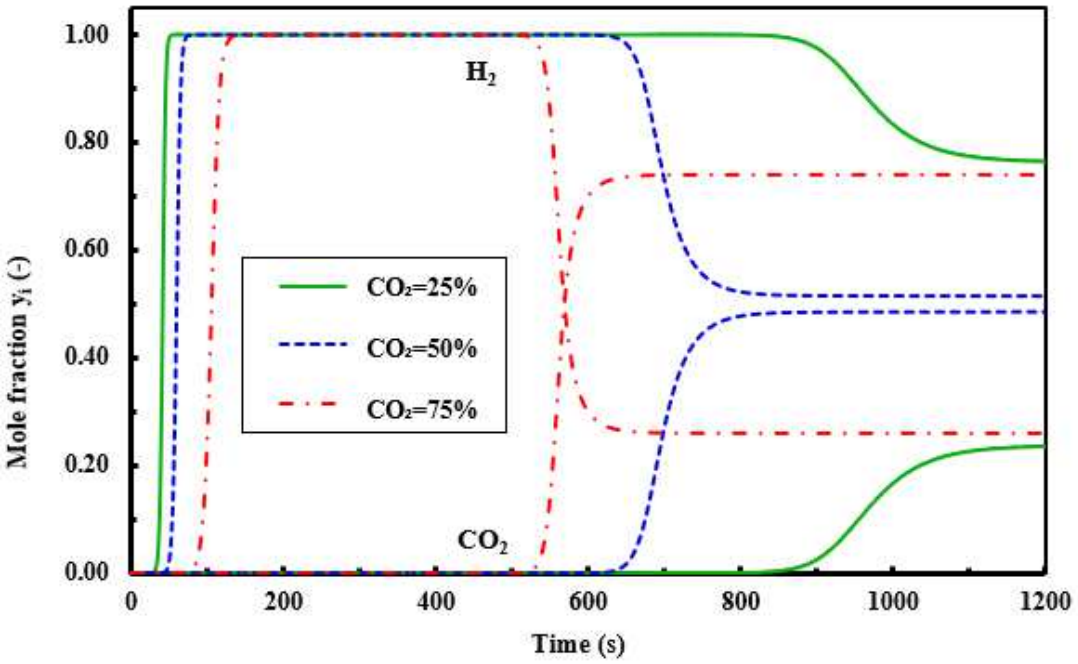


Figure 14 Effect of CO_2/H_2 Feed Ratio on Breakthrough Curves in the Adsorption Bed.

Figure 15 illustrates the effect of inlet gas composition (CO_2/H_2) molar ratio on the amount of CO_2 adsorbed (q_{CO_2}) over time in a fixed-bed adsorption system. The three curves represent CO_2 concentrations of 25%, 50%, and 75% in the feed mixture. All other operating conditions, such as pressure and temperature, are constant. The results clearly demonstrate that increasing the CO_2 content in the feed mixture results in an increased adsorption capacity. At 25% CO_2, the adsorbed amount increases slowly, reaching a lower final value (0.5 mol/kg). As the CO_2 concentration increases to 50% and 75%, both the adsorption rate and final capacity increase significantly, with the adsorbed CO_2 reaching over 0.9 mol/kg at 75%. This trend is expected because higher CO2 partial pressure increases adsorption strength, allowing the adsorbent to adsorb more CO2. Additionally, more CO2 molecules are available to occupy active sites on the adsorbent surface.

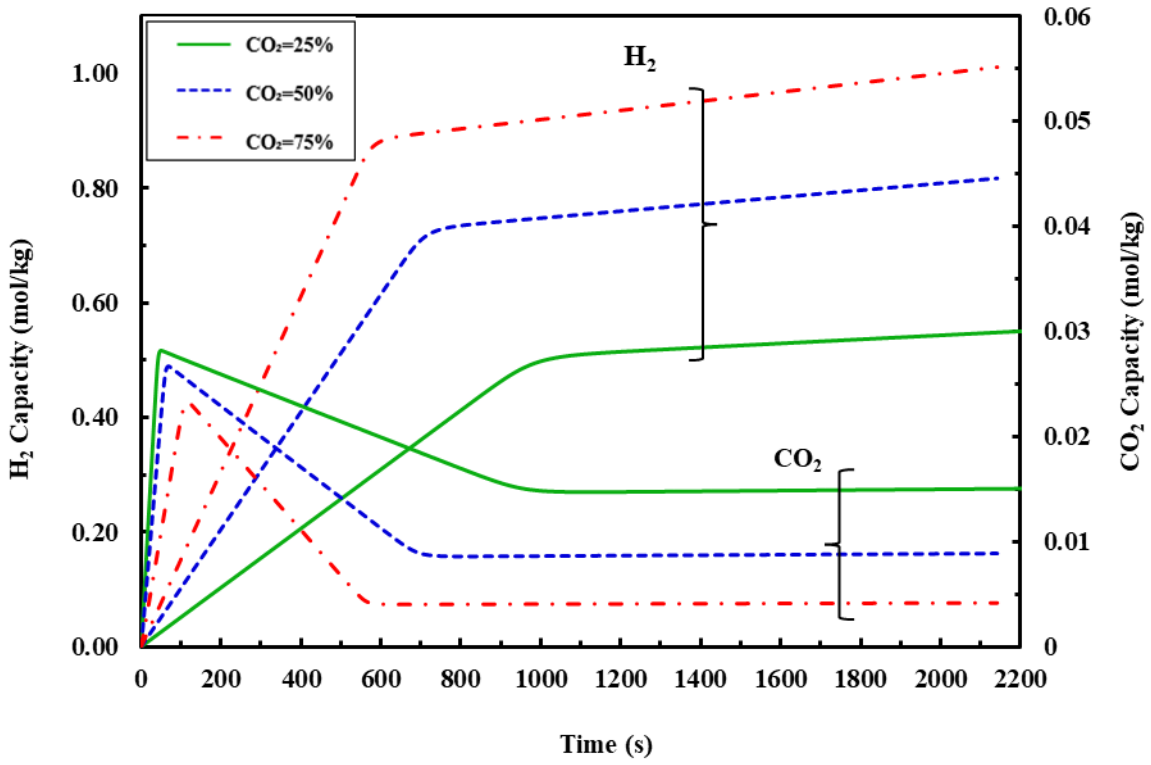


Figure 15. Effect of inlet CO_2 concentration on CO_2 adsorption capacity over time.

5.4 Effect of CO_2/H_2 Gas Hourly Space Velocity (GHSV)

Figure 16 illustrates the effect of GHSV on the exceptional performance of CO_2 and H_2 in a fixed-bed adsorption system. Simulations were conducted at five GHSV values: 100, 200, 300, 400, and 500 h^{-1}, maintaining constant operating conditions of 0 bar, 298 K, and a 50/50 CO2/H2 mole ratio at the inlet. As shown in the figure, increasing the GHSV results in earlier CO_2 penetration and faster saturation of the adsorption bed. At the lowest flow rate (100 h), CO_2 remains adsorbed for a much longer time, and the outlet concentration remains lower for a longer period, indicating improved capture efficiency due to the longer residence time. Conversely, as the GHSV increases, the contact time between the gas and the adsorbent decreases, accelerating the penetration process. This trend reflects known mass-transfer limitations at high flow rates, where rapid gas movement reduces adsorption efficiency. Extending the contact time improves purification efficiency at low GHSV values by facilitating the diffusion of CO_2 into the adsorbent's pores. Conversely, H_2 penetrates the adsorbent earlier at all flow rates due to its weak interaction with it. Therefore, the results demonstrate that while high GHSV conditions impair adsorption performance, a crucial element for maximizing the throughput and efficiency of H_2 purification systems, low GHSV values enhance CO_2 capture efficiency.

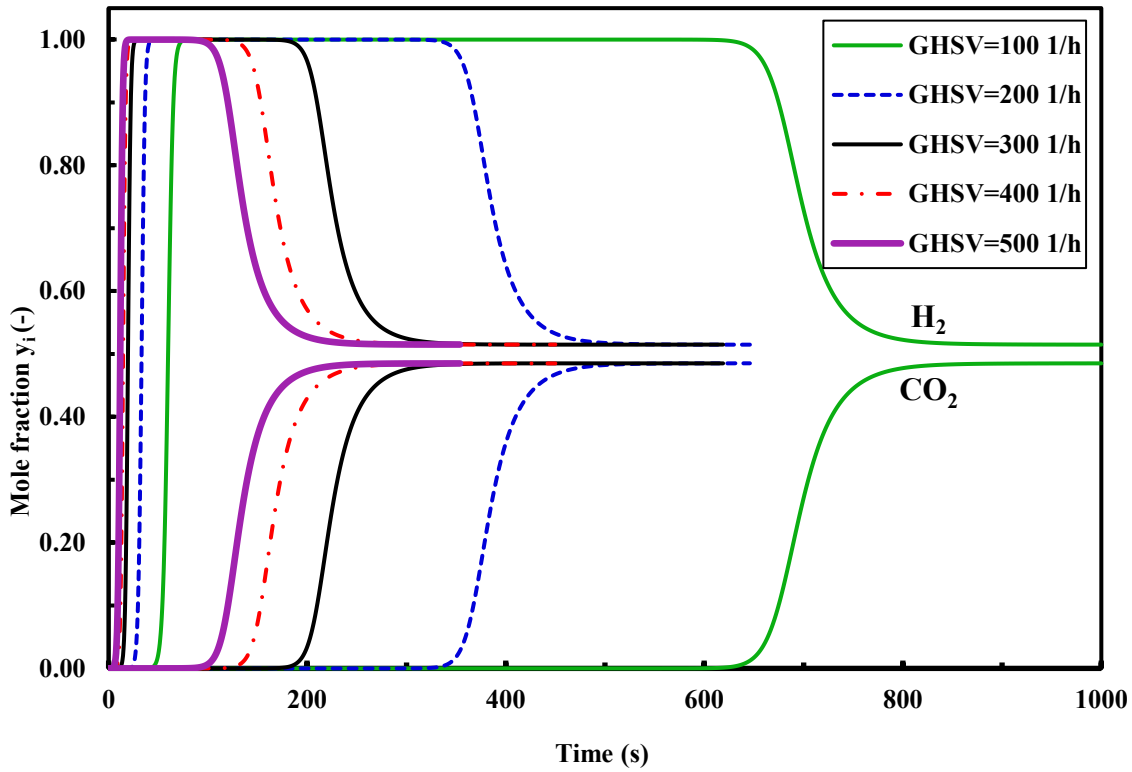


Figure 16 Effect of GHSV on CO_2 and H_2 Breakthrough Curves in the Adsorption Column bed.

This study investigated the key operational factors and their effects on CO_2 adsorption performance. Since adsorption is an exothermic process, a lower inlet temperature (298-448 K) improves CO_2 adsorption. Increasing the adsorption driving force and consequently raising the operating pressure from 0 to 20 bar, also enhances CO_2 uptake. Furthermore, increasing the CO_2 concentration in the feedstock leads to faster saturation of the adsorbent, with the CO_2 to H_2 molar ratio increasing from 25/75 to 75/25. Finally, GHSV values ranging from 100 to 500 h-1 indicate that lower GHSV results in longer contact time between the gas and the adsorbent, thereby improving CO_2 adsorption efficiency. Together, these trends provide valuable guidance for optimizing operating conditions in hydrogen purification systems using adsorption.

According to simulation results, a low adsorption temperature (298 K), high pressure (20 bar), a moderate CO_2/H_2 flow ratio (50/50), and a low GHSV (100 h^{-1}) are the ideal operating conditions for optimizing CO_2 adsorption and extending the lifetime of the adsorption layer. This combination of factors delays CO_2 penetration and improves overall retention efficiency by providing an optimal balance between adsorption strength, residence time, and gas mixture composition. These conditions are ideal for improving CO_2 removal in pre-combustion gas separation applications, while simultaneously enhancing H_2 purification performance.

Figure 17 illustrates the temperature fluctuations within the adsorption layer over time at three different axial positions (x = 0.05 m, x = 0.10 m, and x = 0.15 m). Since the adsorption of CO_2 onto activated carbon in a stationary layer system is exothermic, the data demonstrate the resulting thermal response. Because the inlet region (x = 0.05 m) is the first area to come into contact with the CO_2-rich gas mixture, its temperature rises earlier and peaks more rapidly than at other locations. Moving downstream (x = 0.10 m and 0.15 m), the temperature rise is delayed, indicating the gradual movement of the adsorption front along the layer. The highest temperature is observed at each point shortly after the front arrives, followed by stabilization or a slight decrease as the local adsorption rate decreases. This temperature profile clearly demonstrates the propagation of thermal waves generated by CO_2 adsorption and highlights the importance of position-dependent monitoring and thermal management in adsorption column design.

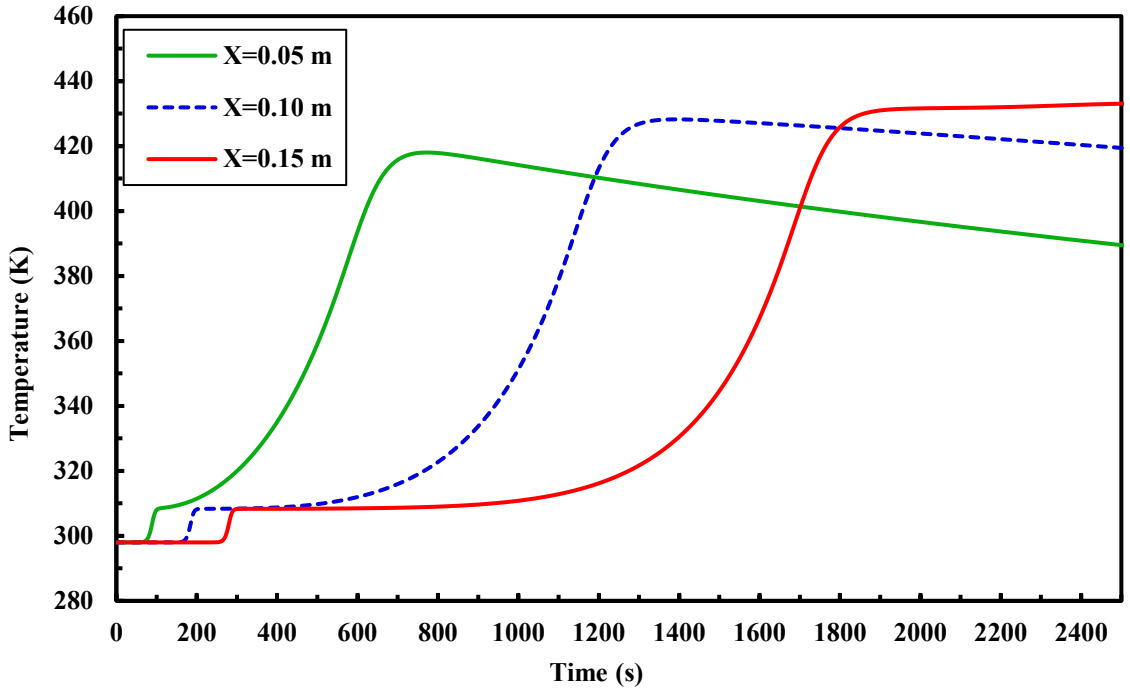


Figure 17. Temperature evolution at different axial positions in the adsorption bed.

Figure 18(A) shows how the CO_2 concentration ($\mathbf{y}_{CO_2}$) changes along the length of the adsorption bed over time. CO_2 is primarily adsorbed near the inlet initially (30 seconds), resulting in a very low concentration throughout the adsorption layer. The color change from blue to green indicates the formation of a distinct adsorption front that progresses toward the outlet over time. The adsorption layer approaches saturation within 1500-2500 seconds, at which point CO_2 begins to appear at the outlet. This development highlights the capacity of the adsorption layer and its dynamic performance by illustrating its penetration behavior and how the adsorption area changes over time. Figure 18(B) shows how the H_2 mole fraction ($\mathbf{y}_{H_2}$) changes along the length of the adsorption bed over time. Initially (at 30 seconds), H_2 is concentrated primarily near the inlet, with only trace amounts present in the rest of the reactor layer. This indicates that H_2 is rapidly leaking

due to its weak adsorption. Over time, hydrogen quickly fills the reactor layer, and its concentration becomes more uniform throughout. By 1000 seconds, the hydrogen content is high in most parts of the layer, and the concentration distribution stabilizes at relatively uniform values across the entire layer after 1500 seconds. This reflects that H_2, being weakly adsorbed, moves freely through the bed and becomes the dominant species at the outlet early in the adsorption process, long before the bed becomes saturated with CO_2.

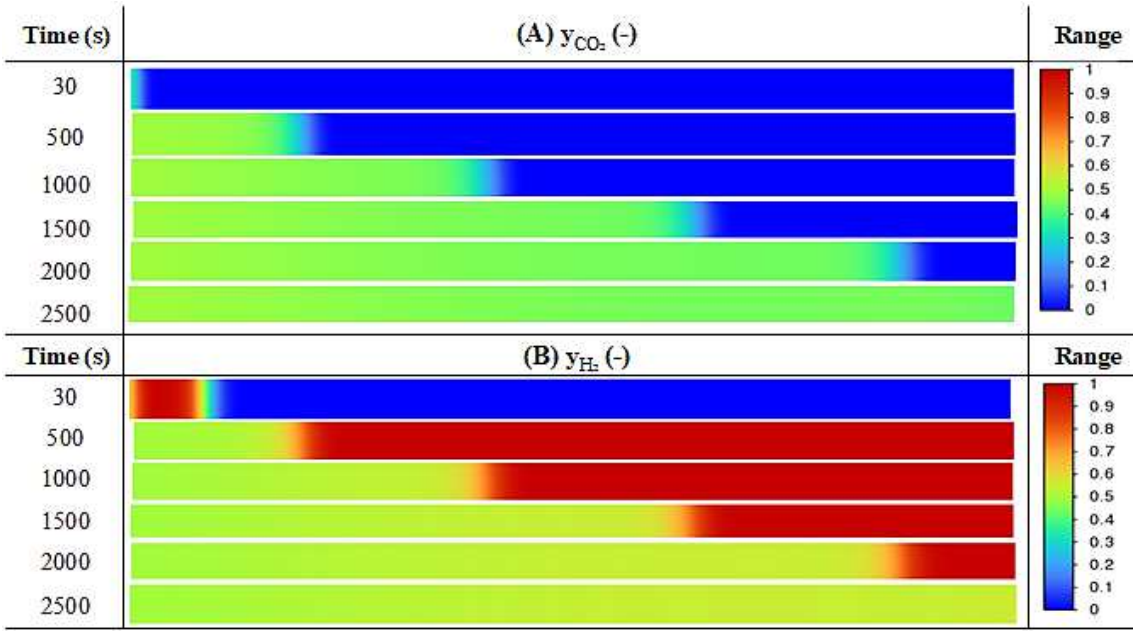


Figure 18. Transient mole fraction profiles (A) CO_2 and (B) H_2 along the adsorption bed at different times.

By analyzing the effects of temperature, pressure, gas composition, and flow rate, optimal conditions for CO_2 capture and H_2 purification were determined from simulation results. Table 5 provides valuable guidance for designing and optimizing adsorption-based separation systems by summarizing key operating parameters.

Table 5. Best-Case Operating Conditions Summary

Parameter	Optimal Value	Effect
Adsorption temperature	298 K	Low temperature improves CO_2 uptake due to its exothermic nature
Adsorption pressure	20 bar	High pressure increases the driving force for CO_2 adsorption
CO_2/H_2 feed ratio	50/50 mol%	Moderate CO_2 content balances capture and bed saturation
GHSV	100 h^{-1}	Low GHSV provides longer residence time for better CO_2 adsorption

From an industrial perspective, the current findings offer valuable guidance for the design of CO_2 units connected to H_2 production facilities after the reforming process. The results demonstrate that feed temperature and operating pressure significantly impact adsorption performance, highlighting the need for efficient heat recovery and gas treatment prior to the adsorption unit.

Adsorption systems may benefit from utilizing existing pressure in industrial reforming processes, thus reducing the need for additional pressure, given the significant improvement in carbon dioxide capture capacity at higher pressures. Moreover, the strong influence of GHSV on breakthrough behavior emphasizes the need to balance productivity and adsorbent utilization during scale-up. Although the current study focuses on a laboratory-scale adsorption column, the trends identified are directly relevant for the design and optimization of industrial fixed-bed and PSA-based hydrogen purification systems.

6. Conclusions

In this study, the behavior of CO_2 and H_2 in a fixed-bed adsorption column filled with activated carbon was simulated using ANSYS Fluent software with custom UDF and UDS codes. The model was validated against published experimental data and included temperature-dependent adsorption, modeled using the Toth equation for CO_2 and the Sips equation for H_2.

The results showed the following:

- Temperature (exothermic adsorption): Lowering T from 448 K to 298 K substantially delays CO_2 breakthrough from 70s to 680 s and increases loading, confirming the strong benefit of cold adsorption fronts.
- Pressure (driving force): Increasing the pressure from 0 to 20 bar changes the breakthrough time from 700 seconds to 2200 seconds and increases the final q_{CO_2} value from 0.75 to 2.4 mol/kg (three times the value), indicating the presence of a specific capacity.
- Feed composition: While a moderate 50/50 mix balances capture time and cycle time, increasing CO_2 at the inlet from 25 to 75 mol% accelerates CO_2 penetration from 850s to 520 s and reduces layer lifetime.
- Flow rate (GHSV): High GHSV reduces the use of mass transfer and contact time; CO_2 breakthrough is compressed from 680 seconds (GHSV=100 h^{-1}) to 100 seconds (GHSV = 500 h^{-1}); and poor adsorption leads to early H_2 breakthrough at all flow rates.
- Best-case window: 298 K, 20 bar, CO_2/H_2 = 50/50, GHSV = 100 h^{-1} maximizes CO_2 capture and extends bed life while preserving H_2's early passage and outlet dominance during adsorption.
- In summary, adsorption temperature, pressure, feed composition, and GHSV play a key role in system performance.
- Model validity: The CFD/UDF framework is suitable for evaluating and designing an integrated SMR-to-adsorption process, and it replicates the literature breakthrough trends for CO_2/H_2 and CO_2/N_2 systems.

The present study has several limitations. The adsorption model assumes fixed-bed operation without cyclic PSA steps, pressure equalization, or adsorbent aging, and assumes a feed after condensation is a binary CO_2/H_2 mixture, omitting trace species (CO, CH_4, etc.) present in industrial reformate. Future work should extend the framework to include full PSA cycle

simulation, multicomponent adsorption, process optimization, and techno-economic assessment to better evaluate commercial feasibility.

Acknowledgment

The authors acknowledge support from King Fahd University of Petroleum & Minerals (KFUPM), Dhahran, Saudi Arabia, through the project DUP2502.

References

[1] H. Karibe, S. Sair, A. Faik, and H. Ait Ousaleh, "Electrified steam methane reforming: A review of heating technologies, challenges, and prospects," *Int. J. Hydrogen Energy*, vol. 133, pp. 200–213, 2025.

[2] R. Kumar and A. Kumar, "Steam reforming of methane and biogas: Thermodynamic and kinetic review for hydrogen production," *Environ. Prog. Sustain. Energy*, vol. 45, no. 2, p. e70345, 2026.

[3] S. Rehman *et al.*, "Techno-economic evaluation and improved sizing optimization of green hydrogen production and storage under higher wind penetration in Aqaba Gulf," *J. Energy Storage*, vol. 99, p. 113368, 2024.

[4] A. Ganguli and V. Bhatt, "Hydrogen production using advanced reactors by steam methane reforming: a review," *Frontiers in Thermal Engineering*, vol. 3, p. 1143987, 2023.

[5] N. Subedi, M. M. H. Bhuiyan, M. A. Islam, B. C. Alfredo, and Z. Siddique, "Hydrogen as an energy carrier: Production pathways, thermochemical constraints, and electrolysis-based green hydrogen prospects," *Int. J. Hydrogen Energy*, vol. 220, p. 154100, 2026.

[6] A. G. H. Saif, A. B. S. Alquaity, and E. M. A. Mokheimer, "Techno-economic analysis of green hydrogen production in Saudi Arabia: A comparative study of solar PV and CSP technologies," *Int. J. Hydrogen Energy*, vol. 105, pp. 1361–1374, 2025.

[7] M. A. Rosen, "Thermodynamic investigation of hydrogen production by steam-methane reforming," *Int. J. Hydrogen Energy*, vol. 16, no. 3, pp. 207–217, 1991.

[8] A. Iulianelli, S. Liguori, J. Wilcox, and A. Basile, "Advances on methane steam reforming to produce hydrogen through membrane reactors technology: A review," *Catalysis Reviews*, vol. 58, no. 1, pp. 1–35, 2016.

[9] S. Nambyaruveettil, L. Ali, and M. Altarawneh, "Green Catalysts for High-Temperature Reactions: Mechanistic Insights and Sustainable Advances in Hydrogenation, Cracking, and Reforming," *The Chemical Record*, vol. 26, no. 5, p. e202500283, 2026.

[10] M. L. Rodriguez, M. N. Pedernera, and D. O. Borio, "Two dimensional modeling of a membrane reactor for ATR of methane," *Catal. Today*, vol. 193, no. 1, pp. 137–144, 2012.

[11] A. N. Allam, N. A. A. Qasem, A. M. Khedr, M. A. Nemitallah, R. Ben-Mansour, and M. A. Habib, "Novel integration of steam-methane reforming with fixed-bed adsorption for efficient blue hydrogen production," *Int. J. Hydrogen Energy*, vol. 247, p. 155720, 2026, doi: https://doi.org/10.1016/j.ijhydene.2026.155720.

[12] L. Chen, Z. Qi, S. Zhang, J. Su, and G. A. Somorjai, "Catalytic hydrogen production from methane: A review on recent progress and prospect," *Catalysts*, vol. 10, no. 8, p. 858, 2020.

[13] A. B. Vakylabad, "Syngas purification by modified solvents with nanoparticles," in *Advances in synthesis gas: methods, technologies and applications*, Elsevier, 2023, pp. 101–130.

[14] J. Wales, D. Hughes, E. Marshall, and P. Chambers, "A review on the application of metal–organic frameworks (MOFs) in pressure swing adsorption (PSA) nitrogen gas generation," *Ind. Eng. Chem. Res.*, vol. 61, no. 27, pp. 9529–9543, 2022.

[15] F. Raganati and P. Ammendola, "CO2 post-combustion capture: a critical review of Current technologies and future directions," *Energy & Fuels*, vol. 38, no. 15, pp. 13858–13905, 2024.

[16] M. Y. Mir, J. A. Parray, and S. Bhattacharya, "Toward Clean Hydrogen: Emerging Carbon Capture and Conversion Technologies in the Energy Transition," *Low-Carbon Hydrogen: Production Technologies and Emerging Applications*, pp. 81–109, 2026.

[17] Y. Wang *et al.*, "A review of CO2 sorbents for promoting hydrogen production in the sorption-enhanced steam reforming process," *Int. J. Hydrogen Energy*, vol. 46, no. 45, pp. 23358–23379, 2021.

[18] E. Kamio, T. Yoshioka, and H. Matsuyama, "Recent advances in carbon dioxide separation membranes: a review," *Journal of Chemical Engineering of Japan*, vol. 56, no. 1, p. 2222000, 2023.

[19] M. H. Zarghampoor, M. Soleimani, M. Mozaffarian, and M. T. Ravanchi, "New hybrid membrane vacuum swing adsorption process for CO2 removal from N2/CO2 mixture:

modeling and optimization by genetic algorithm," *Environmental Science and Pollution Research*, vol. 29, no. 60, pp. 90820–90834, 2022.

[20] M. A. Tabar, H. Maghsoudi, and J. F. M. Denayer, "Hybrid membrane-vacuum pressure swing adsorption: low-cost technology for simultaneous biomethane and carbon dioxide production from biogas," *Bioresour. Technol.*, vol. 422, p. 132241, 2025.

[21] A. Gupta and N. Puri, "Recent advances in hydrogen production using metal organic frameworks and their composites," *Int. J. Hydrogen Energy*, vol. 78, pp. 303–324, 2024.

[22] M. Y. Mir, J. A. Parray, and S. Bhattacharya, "Advanced Metal–Organic Frameworks for Selective Hydrogen Separation and Purification," in *Low-Carbon Hydrogen: Production Technologies and Emerging Applications*, Springer, 2026, pp. 111–132.

[23] P. Cavaliere, "Hydrogen Separation and Purification," in *Water Electrolysis for Hydrogen Production*, Springer, 2023, pp. 509–541.

[24] J. Wales, D. Hughes, E. Marshall, and P. Chambers, "A review on the application of metal–organic frameworks (MOFs) in pressure swing adsorption (PSA) nitrogen gas generation," *Ind. Eng. Chem. Res.*, vol. 61, no. 27, pp. 9529–9543, 2022.

[25] P. Sharma, "Hydrogen Separation and Purification," in *A Textbook on Hydrogen Energy: Production, Storage, Transport and Utilization*, Springer, 2026, pp. 149–169.

[26] A. Krótki, J. Bigda, T. Spietz, K. Ignasiak, P. Matusiak, and D. Kowol, "Performance Evaluation of Pressure Swing Adsorption for Hydrogen Separation from Syngas and Water–Gas Shift Syngas," *Energies (Basel).*, vol. 18, no. 8, p. 1887, 2025.

[27] C. Chilev, M. Dicko, P. Langlois, and F. Lamari, "Modelling of single-gas adsorption isotherms," *Metals (Basel).*, vol. 12, no. 10, p. 1698, 2022.

[28] R. Ben-Mansour and N. A. A. Qasem, "An efficient temperature swing adsorption (TSA) process for separating CO2 from CO2/N2 mixture using Mg-MOF-74," *Energy Convers. Manag.*, vol. 156, pp. 10–24, 2018, doi: https://doi.org/10.1016/j.enconman.2017.11.010.

[29] J. Kim, J. Park, M. Qi, I. Lee, and I. Moon, "Process integration of an autothermal reforming hydrogen production system with cryogenic air separation and carbon dioxide capture using liquefied natural gas cold energy," *Ind. Eng. Chem. Res.*, vol. 60, no. 19, pp. 7257–7274, 2021.

[30] F. V. S. Lopes, C. A. Grande, and A. E. Rodrigues, "Activated carbon for hydrogen purification by pressure swing adsorption: Multicomponent breakthrough curves and PSA performance," *Chem. Eng. Sci.*, vol. 66, no. 3, pp. 303–317, 2011.

[31] S. Ahn, Y.-W. You, D.-G. Lee, K.-H. Kim, M. Oh, and C.-H. Lee, "Layered two-and four-bed PSA processes for H2 recovery from coal gas," *Chem. Eng. Sci.*, vol. 68, no. 1, pp. 413–423, 2012.

[32] J. Schell, N. Casas, R. Pini, and M. Mazzotti, "Pure and binary adsorption of CO 2, H 2, and N 2 on activated carbon," *Adsorption*, vol. 18, pp. 49–65, 2012.

[33] N. Casas, J. Schell, R. Blom, and M. Mazzotti, "MOF and UiO-67/MCM-41 adsorbents for pre-combustion CO2 capture by PSA: Breakthrough experiments and process design," *Sep. Purif. Technol.*, vol. 112, pp. 34–48, 2013.

[34] S. G. Subraveti *et al.*, "Cycle design and optimization of pressure swing adsorption cycles for pre-combustion CO2 capture," *Appl. Energy*, vol. 254, p. 113624, 2019.

[35] A. Streb and M. Mazzotti, "Adsorption for efficient low carbon hydrogen production: part 1—adsorption equilibrium and breakthrough studies for H 2/CO 2/CH 4 on zeolite 13X," *Adsorption*, vol. 27, pp. 541–558, 2021.

[36] N. Zhang, P. Benard, R. Chahine, T. Yang, and J. Xiao, "Optimization of pressure swing adsorption for hydrogen purification based on Box-Behnken design method," *Int. J. Hydrogen Energy*, vol. 46, no. 7, pp. 5403–5417, 2021.

[37] N. Zhang, S. Hu, and Q. Xin, "Optimization of pressure swing adsorption in a three-layered bed for hydrogen purification using machine learning model," *Sci. Rep.*, vol. 15, no. 1, p. 14193, 2025.

[38] A. N. Allam, M. A. Nemitallah, M. A. Habib, N. A. Qasem, and A. S. Farooqi, "Enhancing Hydrogen Production in a Porous Reactor for the Steam Methane Reforming: Optimizing Operating Parameters and Radiation Heat Transfer Mechanism," *ASME Open Journal of Engineering*, vol. 4, 2025.

[39] A. Fluent, "Ansys fluent theory guide," *Ansys Inc., USA*, vol. 15317, pp. 724–746, 2011.

[40] T. P. Tiemersma, C. S. Patil, M. van Sint Annaland, and J. A. M. Kuipers, "Modelling of packed bed membrane reactors for autothermal production of ultrapure hydrogen," *Chem. Eng. Sci.*, vol. 61, no. 5, pp. 1602–1616, 2006.

[41] J. Xiao, R. Peng, D. Cossement, P. Bénard, and R. Chahine, "CFD model for charge and discharge cycle of adsorptive hydrogen storage on activated carbon," *Int. J. Hydrogen Energy*, vol. 38, no. 3, pp. 1450–1459, 2013.

[42] R. Ben-Mansour and N. A. A. Qasem, "An efficient temperature swing adsorption (TSA) process for separating CO2 from CO2/N2 mixture using Mg-MOF-74," *Energy Convers.*

Manag., vol. 156, pp. 10–24, 2018, doi: https://doi.org/10.1016/j.enconman.2017.11.010.

[43] J. A. Mason, K. Sumida, Z. R. Herm, R. Krishna, and J. R. Long, "Evaluating metal–organic frameworks for post-combustion carbon dioxide capture via temperature swing adsorption," *Energy Environ. Sci.*, vol. 4, no. 8, pp. 3030–3040, 2011.

[44] R. Sips, "On the structure of a catalyst surface," *J. Chem. Phys.*, vol. 16, no. 5, pp. 490–495, 1948.

[45] D. M. Ruthven, S. Farooq, and K. S. Knaebel, *Pressure swing adsorption*. John Wiley & Sons, 1996.

[46] T. L. P. Dantas *et al.*, "Carbon dioxide–nitrogen separation through adsorption on activated carbon in a fixed bed," *Chemical Engineering Journal*, vol. 169, no. 1, pp. 11–19, 2011, doi: https://doi.org/10.1016/j.cej.2010.08.026.

[47] W. He, W. Lv, and J. H. Dickerson, "Gas Diffusion Mechanisms and Models," in *Gas Transport in Solid Oxide Fuel Cells*, W. He, W. Lv, and J. Dickerson, Eds., Cham: Springer International Publishing, 2014, pp. 9–17. doi: 10.1007/978-3-319-09737-4_2.

[48] F. P. Incropera and D. P. De Witt, "Fundamentals of heat and mass transfer," 1985.

[49] N. Casas, J. Schell, R. Pini, and M. Mazzotti, "Fixed bed adsorption of CO2/H2 mixtures on activated carbon: experiments and modeling," *Adsorption*, vol. 18, no. 2, pp. 143–161, 2012.